A Novel Deformable Phantom for 4D Radiotherapy Verification

Monica Margeanu

Master of Science

Medical Physics Unit

McGill University
Montreal, Quebec
July 2007

A thesis submitted to McGill University in partial fulfilment of the requirements of the degree of Master of Science in Medical Radiation Physics

©Monica Margeanu 2007



Library and Archives Canada

Published Heritage Branch

395 Wellington Street Ottawa ON K1A 0N4 Canada Bibliothèque et Archives Canada

Direction du Patrimoine de l'édition

395, rue Wellington Ottawa ON K1A 0N4 Canada

> Your file Votre référence ISBN: 978-0-494-38420-6 Our file Notre référence ISBN: 978-0-494-38420-6

NOTICE:

The author has granted a non-exclusive license allowing Library and Archives Canada to reproduce, publish, archive, preserve, conserve, communicate to the public by telecommunication or on the Internet, loan, distribute and sell theses worldwide, for commercial or non-commercial purposes, in microform, paper, electronic and/or any other formats.

AVIS:

L'auteur a accordé une licence non exclusive permettant à la Bibliothèque et Archives Canada de reproduire, publier, archiver, sauvegarder, conserver, transmettre au public par télécommunication ou par l'Internet, prêter, distribuer et vendre des thèses partout dans le monde, à des fins commerciales ou autres, sur support microforme, papier, électronique et/ou autres formats.

The author retains copyright ownership and moral rights in this thesis. Neither the thesis nor substantial extracts from it may be printed or otherwise reproduced without the author's permission.

L'auteur conserve la propriété du droit d'auteur et des droits moraux qui protège cette thèse. Ni la thèse ni des extraits substantiels de celle-ci ne doivent être imprimés ou autrement reproduits sans son autorisation.

In compliance with the Canadian Privacy Act some supporting forms may have been removed from this thesis.

While these forms may be included in the document page count, their removal does not represent any loss of content from the thesis.

Conformément à la loi canadienne sur la protection de la vie privée, quelques formulaires secondaires ont été enlevés de cette thèse.

Bien que ces formulaires aient inclus dans la pagination, il n'y aura aucun contenu manquant.



ACKNOWLEDGEMENTS

First, I would like to express my gratitude to my thesis supervisors, *Dr. Jan Seuntjens* and *Dr. Gabriela Stroian*. Thank you for your guidance, support, patience and encouragement during the preparation of this thesis, for always being willing to help me with whatever problem I had.

I also wish to thank *Emily Heath* for her great help with deformable image registration and many discussions on phantom construction.

I would like to acknowledge *Robin Van Gils* for helping with the construction of the phantom and for teaching me the basics and operation rules of the mechanical workshop.

I am grateful to Joe Larkin, Bavan Sivagnanam and Pierre Léger for helping with the automation and making the phantom "breathe".

My sincere appreciation goes to all staff of the McGill Medical Physics Unit. In particular I would like to thank *Dr. Ervin Podgorsak*, the head of the department, for developing such an excellent program and allowing me to study in the department of Medical Physics. Also a special thanks goes to *Margery Knewstubb* for her kind assistance and advice in dealing with administrative issues.

I also thank all of my classmates and friends for all of the good times that we have shared during our studies in Montréal.

Finally, I would like to express my deepest gratitude to my parents for their love and support, both moral and financial, without which this thesis would not be.

ABSTRACT

The goal of conformal radiation techniques is to improve local tumour control through dose escalation to target volumes while at the same time sparing surrounding healthy tissue. Respiratory motion is known to be the largest intra-fractional organ motion and the most significant source of uncertainty in treatment planning for chest lesions. A method to account for the effects of respiratory motion is to use four-dimensional radiotherapy. While analytical models are useful, it is essential that the motion problem in radiotherapy is addressed by both modeling as well as experimentally studies so that different obstacles can be overcome before clinical implementation of a motion compensation method. Validation of techniques aimed at measuring and minimizing the effects of respiratory motion require a realistic dynamic deformable phantom for use as a gold standard. In this work we present the design, construction, performance and deformable image registration of a novel breathing, tissue equivalent phantom with a deformable lung that can reproducibly emulate 3D non-isotropic lung deformations according to any real lung-like breathing pattern. The phantom consists of a Lucite cylinder filled with water containing a latex balloon stuffed with dampened natural sponges. The balloon is attached to a piston that mimics the human diaphragm. Nylon wires and Lucite beads, emulating vascular and bronchial bifurcations, were glued at various locations, uniformly throughout the sponges. The phantom is capable of simulating programmed irregular breathing patterns with varying periods and amplitudes. A deformable, tissue equivalent tumour, suitable for holding radiochromic film for dose measurements was embedded in the sponge. Experiments for 3D motion assessment, motion reproducibility as well as deformable image registration and validation are presented using the deformable phantom.

ABRÉGÉ

Le but des techniques de radiation conformationnelle est d'améliorer le contrôle de la tumeur locale par escalade de dose aux volumes cibles tout en préservant les tissus sains environnants. Le mouvement respiratoire est connu pour être le mouvement intra-fractionnel d'organe le plus important et la source d'incertitude la plus élevée pour les plans de traitement des lésions de poitrine. Une méthode pour prendre en compte les effets du mouvement respiratoire est d'utiliser la radiothérapie quatre dimensions. Bien que les modles analytiques soient utiles, il est essentiel de traiter les problmes de mouvement en radiothérapie par la fois des études numériques et expérimentales afin que les différents obstacles puissent être dépassés avant l'implémentation clinique d'une méthode de compensation du mouvement. La validation des techniques dont le but est de mesurer et de minimiser les effets du mouvement respiratoire nécessite un fantôme réaliste dynamique déformable pour une utilisation en tant que "gold standard". Dans ce travail, nous présentons le concept, la construction, la performance et l'enregistrement d'image déformable d'un nouveau fantôme respiratoire équivalent tissu avec un poumon déformable qui peut imiter de manire reproductible les déformations 3D non-isotropiques du poumon selon le comportement respiratoire d'un poumon réel. Le fantôme consiste en un cylindre de Lucite rempli d'eau contenant un ballon en latex, lui-même rempli d'éponges humides naturelles. Le ballon est attaché un piston qui simule le diaphragme humain. Des fils de Nylon et des perles de Lucites, simulant les bifurcations vasculaires et bronchiales, étaient collés différentes positions, uniformément travers les éponges.

Le fantôme est capable de simuler des comportements respiratoires irréguliers programmés avec des périodes et des amplitudes différentes. Une tumeur déformable équivalent tissu, appropriée pour les films radiochromiques utilisés pour la mesure de dose, a été insérée dans l'éponge. Les expériences pour les tests de mouvement 3D, la reproductibilité du mouvement, l'enregistrement d'image déformable et la validation sont présentées en utilisant le fantôme déformable du poumon.

TABLE OF CONTENTS

ACK	NOWI	LEDGEMENTS	ii
ABS'	TRAC	Г	iii
ABR	ÉGÉ .		v
LIST	OF T	ABLES	ix
LIST	OF F	IGURES	x
1	Introd	luction	1
	1.1 1.2 1.3 1.4	Modern approaches to radiation therapy	1 3 7 9
2	Conce	pts and Implementation of Four-Dimensional Radiation Therapy .	12
	2.1 2.2 2.3	4D Computed tomography	12 19 23
3	Image	Registration Techniques	25
	3.1 3.2 3.3	Classification of registration methods	26 29 30 30 36
	3.4	The ANIMAL non-linear registration algorithm	37 38 39 42

		3.4.4 Optimization method	46
4	Phant	som-based Verification Methods for Motion Management	50
	4.1 4.2 4.3	Ideal lung phantom: the human lung Literature review on existing phantoms	50 55 61
5	_	n, Construction and Performance of a Novel Deformable Lung	63
	5.1 5.2 5.3 5.4 5.5 5.6 5.7	Phantom construction Simulation of lung tissue CT data acquisition Performance of the deformable lung phantom Assessment of 3D motion and motion reproducibility Deformable image registration Accuracy of deformable image registration	63 64 66 68 70 72 76
6	Concl 6.1 6.2	Summary of the work performed	83 84 86
REF	FEREN	CES	88
Inde	ex		101
List of Abbreviations			

LIST OF TABLES

<u>Table</u>		<u>pa</u>	age
3–1	Common image similarity measures used in registration		32
4–1	Mean range of lung tumour-motion data		53
5–1	Mean mass densities in 4D CT imaged patients and lung phantom $$.		70
5–2	Differential motion of different landmarks under compression		74
5–3	Accuracy of DIR at $0.7 \text{x} 0.7 \text{x} 1.25 \text{ mm}^3$ image resolution		78
5-4	Tumour and lung 3D mean DTAs and COM shifts		80
5-5	Accuracy of DIR at 0.7x0.7x3 mm ³ image resolution	•	81

LIST OF FIGURES

Figure	I	oage
1–1	CT motion artifacts	4
1–2	Blurring effect of motion during static dose delivery	5
1-3	Interplay effect of motion during dynamic dose delivery	6
2-1	Amplitude-based sorting 4D CT scans using ciné acquisition	14
2-2	Phase-based sorting 4D CT scans using helical acquisition	15
2-3	Amplitude and phase labeling in 4D	16
2-4	Phase-based sorting	17
2-5	Amplitude versus phase-angle sorting	19
2–6	Free breathing versus respiratory gated CT scans	20
2-7	4D treatment planning flow chart	21
2-8	Superposition of target and beam motion in 4D TD	24
2-9	Adaptive versus static delivery	24
3-1	Schematic draw of rigid and non-rigid registration	27
3-2	Blur image intensity and image gradient magnitude data	39
3–3	Non-linear deformation field	43
3-4	Deformation lattice grid definition	43
3-5	Local node deformation strategy	48
4-1	Patient respiratory patterns	52
4-2	Tumour trajectories in 23 lung patients	55

4–3	Deformable lung phantom designed by D'Souza et al	56
4–4	Experimental setup of Rando phantom designed by D'Souza $\it et~\it al.~$	57
4-5	Deformable phantom designed by Lu et al	58
4-6	Deformable lung phantom designed by Nioutsikou et al	59
4–7	Deformable lung phantom designed by Kashani et al	60
4-8	CIRS Model Dynamic Thorax Phantom	61
5–1	Prototype of the deformable phantom designed at MGH	64
5–2	Principle of deformable lung inflation	65
5-3	Lung tissue simulation	67
5-4	CT number histograms in a real and phantom lung	69
5-5	Example of manually chosen point landmarks	71
5-6	3D motion assessment	73
5-7	Tumour 3D triangulated surfaces	78
5-8	Tumour colour-coded representation of DTA	80
5-9	Red-green image fusion	82

CHAPTER 1 Introduction

1.1 Modern approaches to radiation therapy

Radiation therapy is the medical use of ionizing radiation, most commonly consisting of photons and electrons, as part of cancer treatment to control malignant cells. Radiotherapy may be used as the primary therapy and can also be combined with surgery, chemotherapy, hormone therapy or some mixture of the three. The damage to cancerous cells is related to the absorbed dose (*i.e.*, energy absorbed from ionizing radiation per unit mass) and therefore by increasing the dose to the tumour, the number of killed cancer cells increases and so does the probability of cure.

Despite promising molecular work on radiation sensitivity, patients with primary tumour confined to its loco-regional site are currently treated with three-dimensional conformal radiotherapy (3D CRT) where a high dose region is adjusted around the target volume while delivering as low as possible a dose outside. This technique relies on accurate target definitions, dose planning and delivery in order to increase local tumor control probability (TCP) and/or decrease normal tissue complication probability (NTCP). The impact of 3D CRT may be a 10-20 increase in 5-year survival rate [105, 118] but its success may be compromised by errors in target location as well as discrepancies between planned and delivered dose distributions. Major contributors to these errors are the limitations of anatomical image modalities for

complete target characterization and localization, the clinical use of inadequate dose calculation algorithms and the disregard of respiratory motion.

The development of the intensity-modulated radiation therapy (IMRT) techniques allows for planning and delivering radiation treatments with higher dose gradients and tighter treatment margins than possible with conventional irradiation techniques [119, 14, 82, 21]. With the IMRT technique, using multiple intensity modulated beams, one can deliver a high dose of radiation to the target and a low dose to the surrounding normal structures. IMRT planning provides improved tumor target conformity when compared to 3D CRT treatment planning. There is significant sparing of critical structures and other normal tissues. However, reducing the treatment margins without an associated improvement in patient setup, immobilization, and localization may result in an unintentional underdosing of the target volume, and therefore increase the risk of local tumor recurrence. Therefore, there is concern that highly conformal therapy, such as IMRT, designed based on a single computed tomography (CT) dataset acquired for planning purposes may lead to marginal misses of target volumes [36, 56]. In addition, the locations, shapes, and sizes of the tumor(s) and normal anatomy have been found to change significantly due to daily positioning uncertainties and physiological and/or clinical factors during the course of radiation treatments. The latter includes inter-fraction motion/deformation that occurs on a fraction-to-fraction level such as tumor shrinkage, weight loss, variations in rectal and bladder contents or intra-fraction motion/deformation that occurs while the patient is being irradiated and which are caused by the respiratory, skeletal, muscular, cardiac and gastrointestinal systems.

A new approach that accounts for the intra- and inter-fraction motion/deformation is the use of the *image-guided radiotherapy* (IGRT). IGRT is an application of dynamic feedback control in radiation treatment that utilizes the image feedback of patient-specific anatomical and biological variations to frequently evaluate treatment quality and to optimize the treatment plan if necessary by including the variations in the design of dose distribution. Practitioners are using new image-guided techniques to verify the tumor location each day. *Ultrasound* systems have begun to find their way into the clinic, but they only work well in the abdomen where there are no air cavities or significant amounts of bone. An alternative approach is *electronic portal imaging*, which requires the placement of small, inert marker seeds in the soft-tissue tumor as an aid to visualization. Yet another technique is to produce a CT image of the patient using the "cone beam" technique. The linear accelerator's larger conical beam is used, and the entire 3D volume can be imaged with just one linac rotation. The cone-beam approach works for either kV or MV X-ray beams, but a kV beam produces the highest image quality using the least amount of dose.

1.2 Effects of respiratory motion in conventional radiation therapy

The newest challenge in modern, 3D CRT and IMRT is to deliver the prescribed dose distribution to a moving, deformable target. If the respiratory motion is not accounted for, during conventional radiotherapy for thoracic and abdominal sites, imaging, planning and delivery errors can be introduced.

For instance, a conventional CT scan represents anatomic information acquired from various phases of the respiration cycle and can include severe motion artifacts.

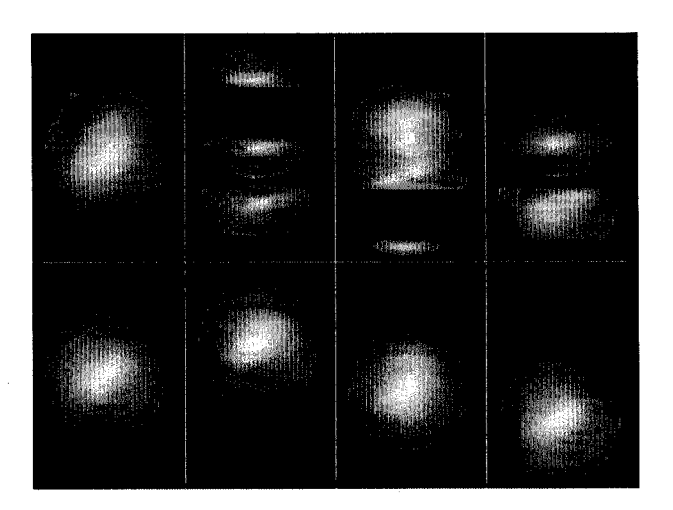


Figure 1–1: Isosurface renderings of a spherical object CT scanned while periodically moving on a sliding table. Top row: different artifacts obtained by axial CT scanning. Bottom row: left shows a CT scan of the static object. Other images show three positions of the sphere while moving as imaged with four-dimensional computed tomography (4D CT) which is described in *Section 1.3*. Reproduced from [86].

This makes target delineation inaccurate on planning CT images, which results in incorrect anatomical position, volume and shape of the tumour (Fig. 1–1).

Also, the conventional treatment planning for mobile lung tumours based on a single CT scan acquired under quiet free breathing, leads to suboptimal dose calculation. During treatment planning the margins around the tumour need to be large enough to ensure coverage of the target at full extents of motion. Generally, for CT-planned lung cancer treatments, the gross tumour volume (GTV) is outlined and a margin is added to include the suspect microscopic spread (which when added to the GTV creates the clinical target volume (CTV)). To obtain the planning target volume (PTV) from the CTV involves adding margins to account for intra-fraction motion, inter-fraction motion and setup error. Nevertheless, the volume actually treated is

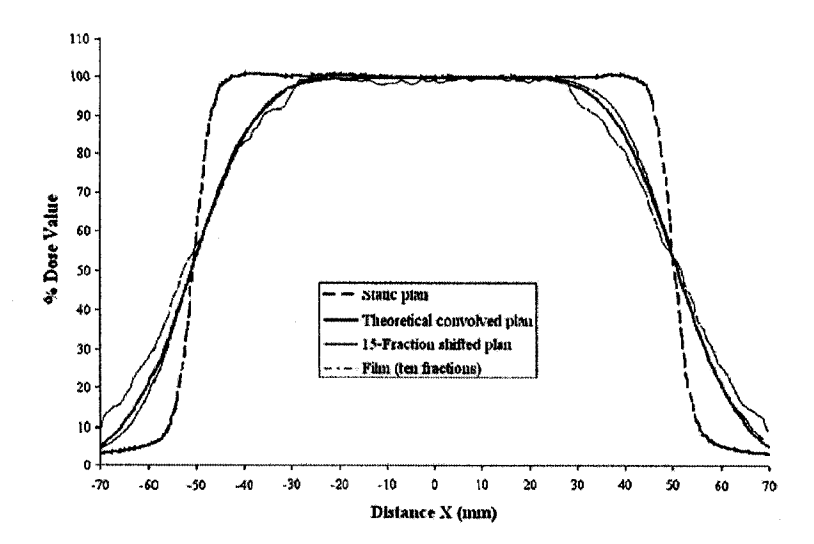


Figure 1–2: Motion during static dose delivery leads to a blurred dose distribution: solid water phantom, irradiated with 10 photon beams, shifted along a line parallel to the phantom surface according to a Gaussian distribution with a standard deviation $\sigma = 10$ mm. Reproduced from [9].

usually larger and there is an even larger volume of tissue irradiated to a dose considered significant in relation to normal tissue tolerance. Because of the artifacts observed in CT images in which respiratory motion has not been accounted for, the magnitude of margin to allow for respiratory motion is difficult to quantify. Adding treatment margins increases the volume of healthy tissue exposed to significant doses and hence increases the likelihood of treatment-related complications.

Radiation delivery in the presence of intra-fraction organ motion causes an averaging or blurring effect of the static dose distribution over the path of the motion while inter-fraction motion causes a shift of the dose distribution. The amount of blurring depends on the amplitude and the characteristics of the motion and on the

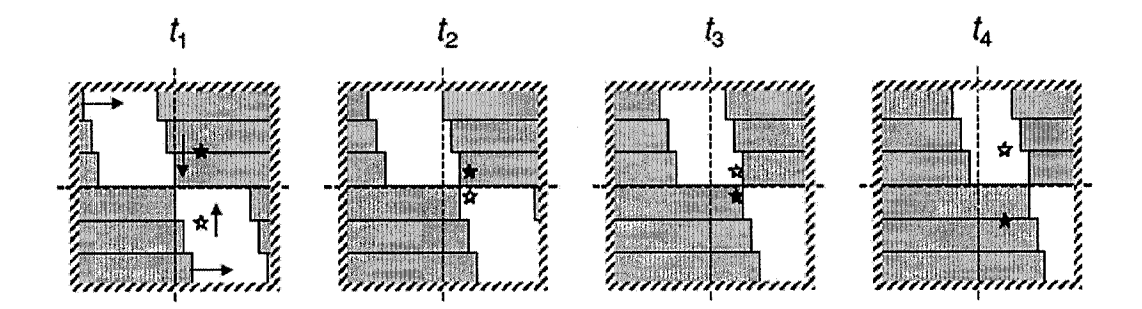


Figure 1–3: The leaves move from left to right. The star symbolizes a point in an organ that moves up and down and the two different types of stars represent two different phases of the motion. Depending on the phase relative to the leaf motion, the point can receive very different dose values. Reproduced from [68].

sharpness of the static dose distribution but it does not depend on the specific delivery technique. The blurring leads to an enlarged penumbra at the field edge and thus to a less conformal dose distribution (Fig. 1–2). During dynamic delivery (i.e., beam-shaping aperture moves during dose delivery) there is a blurring effect (due to organ motion) but also the so-called interplay effect. The interplay effect is caused by the combination of the intra-fraction target motion and the beam motion which generates variations of the dose in each voxel. An illustration of the interplay effect in the case of multileaf collimator (MLC) delivery is shown in Fig. 1–3. The two previous effects assume that the dose distribution is invariant to displacements of the internal structure of the patient. This assumption would be valid only if the density of the organs were uniform. However, at interfaces between structures of different densities and/or atomic numbers, there are interface phenomena that affect the dose distribution locally. This interface effects move with moving interfaces and can lead to distortions in the dose distributions.

1.3 Overview of methods to account for respiratory motion

Because intra-fraction organ motion can be substantial, with resultant alterations in organ volume definition and dosimetry, interventions to reduce it are required for many patients if dose escalation and reduction of dose to normal tissue are the treatment goals.

The simplest approach to reduce dose margins and dose targeting error associated with breathing is by using methods that minimize the breathing motion itself, and an easy way to do this is by educating the patient to breath in a shallow breathing pattern (voluntary shallow breathing). Jet ventilation, abdominal belts and stereotactic frames that produce firm abdominal pressure have also been used to reduce the respiratory motion of upper abdominal organs (forced shallow breathing) [7, 53, 54].

Another simple way to minimize the breathing motion is via breath holding and this can be done passively (voluntary breath hold) [4] or actively (forced breath hold or active breathing control (ABC)) [83, 115] and has been shown to reduce lung tumour position uncertainties to a few milimiters. Breath holding involves administration of radiation (during both imaging and treatment delivery) within a particular, reproducible portion of the patient breathing cycle, usually chosen as deep-inspiration. The applicability of this method is limited by patient ability to hold breath comfortably for at least 20 seconds and requires longer simulation and treatment times.

If the patient breathing cannot be regulated, the imaging and the external beam exposure can be synchronized with part of the breathing cycle where tumour motion is minimal (respiratory gating), commonly referred to as the "gate" [98, 100].

The position and gate within a respiratory cycle are determined by monitoring the patient's respiratory motion, using either an external respiration signal or internal fiducial markers. As the beam is not continuously delivered, gated procedures are longer than non-gated procedures.

A different strategy for managing respiration in radiation treatments is by using methods that incorporate the breathing motion into radiotherapy treatment planning. One solution is acquiring slow CT scans that capture the full extent of movement by using long scan times which are of the order of the period of the breathing motion [52, 109]. Another approach to obtaining a tumour-encompassing volume is to acquire both inhalation and exhalation gated or breath-hold CT scans of the patient. Taking both inhalation and exhalation CT scans will more than double the CT scanning time and relies on the patient's ability to hold his or her breath reproducibly. The two scans require image fusion and extra contouring. The advantage of this approach over the slow scanning method is that the blurring caused by the motion present during free breathing is significantly reduced.

A more complex approach to incorporate the breathing motion into radiotherapy is the four-dimensional radiotherapy (4D RT), where temporal changes in anatomy are taken into account during the imaging, planning and delivery steps of radiotherapy. The four-dimensional computed tomography (4D CT) technology made possible the generation of sequential image datasets for multiple phases of the breathing cycle. The four-dimensional treatment planning (4D TP) designs different treatment plans on each available CT dataset and the accumulation of doses on the planning CT dataset is accomplished by using deformable image registration (DIR). DIR is

an essential tool in the calculation of dose distributions in the presence of motion, where different respiratory states must be registered to a reference volume to track dose delivered to individual voxels. In a full 4D RT approach, such a treatment plan strategy is followed by an adaptive four-dimensional treatment delivery (4D TD) or real-time tumour tracking, in which each plan is delivered when the patient is at the corresponding breathing phase. The 4D approach to radiotherapy method will be detailed in Chapter 2.

1.4 Objectives and structure of this thesis

The motivation of this thesis stems from the need to investigate and minimize the impact of organ motion and patient positioning errors in radiation therapy. The use of patient studies for the purpose of dynamic imaging and targeting techniques verification is not always well suited since ground truth in patient studies is not known. While analytical models are useful, it is essential that the motion problem in radiotherapy is addressed by both modeling as well as experimental studies so that different obstacles can be overcome before clinical implementation of a motion compensation method. Therefore, a reproducible, tissue-equivalent deformable phantom is critical to proper commissioning and use of new systems for physiological motion management in radiation therapy. These difficulties result in the following problem statement:

Problem: Design and evaluate the feasibility of a dynamic deformable, tissue equivalent lung phantom with the initial goal of developing a reliable tool suitable for quality assurance of respiratory gating technique and all aspects of 4D radiation therapy that includes imaging, treatment planning and treatment delivery.

In this thesis we have addressed the following specific aims:

Specific Aims:

- 1. Develop and construct a deformable, tissue equivalent lung phantom that can emulate the 3D non-isotropic motion/deformation of a real lung.
- 2. Assess the 3D motion of the phantom, emphasizing differential motion of various points under compression as well as reproducible configuration at the same amount of compression (breathing state).
- 3. Perform deformable image registration (DIR) between different breathing states of the phantom (e.g., deep inhalation and deep exhalation).
- 4. Assess the accuracy of the deformable image registration using both qualitative and quantitative methods.

This work is structured in two main parts. The first part consists of an extensive review of 4D RT (*Chapter 2*), image registration techniques (*Chapter 3*) as well as a summary of existing phantoms used in motion management in radiotherapy (*Chapter 4*). The second part describes the design, performance and image registration of the proposed deformable lung phantom (*Chapter 5*).

Chapter 2 describes how respiratory motion is accounted for by using 4D RT. The 4D approach to accounting for temporal anatomical changes during imaging, planning and delivery of the radiation is detailed in Sections 2.1 to 2.3.

A new element introduced by 4D TP is the deformable image registration. An overview of image registration techniques as well as an extensive description of the image registration algorithm (ANIMAL) we have used for the deformable image registration of the developed lung phantom are given in *Chapter 3*.

Chapter 4 summarizes existing rigid and deformable phantoms used in motion mitigation techniques and their limitations. The mechanics of breathing and magnitude of the respiratory motion, used as a starting point in the design of an "ideal" deformable lung phantom, are also presented as a comparison.

Chapter 5 describes the design, construction, performance and image registration of the developed deformable lung phantom. The design is presented in Sections 5.1 and 5.2, CT data acquisition and 3D motion assessment in Sections 5.3 to 5.5 and deformable image registration and validation in Sections 5.6 and 5.7.

The thesis ends with conclusions and suggestions for further work that are offered in *Chapter 6*.

CHAPTER 2

Concepts and Implementation of Four-Dimensional Radiation Therapy

In the past few years, the development of the 4D CT scanning technology allowed the generation of sequential image datasets for multiple phases of the breathing cycle [110]. Integration of similar concepts and tools into radiation therapy has led to the concept of four-dimensional radiotherapy (4D RT), defined as the "explicit inclusion of the temporal changes of anatomy during the imaging, planning and delivery of radiotherapy" [40]. Within such a regimen, tumour motion could be accommodated, for example, by tracking tumours in real time and adjusting the beam delivery accordingly, based on plans individually designed for each available instance of the patient anatomy encountered during a respiratory cycle. The purpose of this chapter is to present the concepts and implementation of 4D RT throughout its three stages: four-dimensional computed tomography (4D CT), four-dimensional treatment planning (4D TP) and four-dimensional treatment delivery (4D TD).

2.1 4D Computed tomography

Generally speaking, CT datasets with minimal motion artifacts can be acquired in three ways: (1) using techniques that shorten the scanner rotation times during image acquisition (i.e., fast scanning); (2) using prospective gating to obtain CT image data sets at only those breathing phases chosen prior to scanning the patient (i.e., respiratory gating); (3) using retrospective gating to obtain CT image data sets for multiple respiratory phases (i.e., 4D CT).

In order to obtain a 4D CT dataset, as the patient is scanned, a respiration signal is simultaneously acquired and at the end of the scan the images are post-processed into individual 3D image datasets according to the respiratory phase at the time each image was acquired.

The respiration signal can be acquired by tracking a surrogate of respiration-related organ and tumor motion: tidal volume (internal lung air content) measured with a spirometer; chest expansion monitored by a pneumatic bellows; motion of a reflecting external marker placed on the abdomen and tracked with a video camera, e.g., Varian's Real-time Position Management (RPM) Respiratory Gating System.

Acquisition Methods: 4D CT dataset acquisition can be conducted using either serial (ciné) or helical scanning.

Ciné scanning consists of acquiring a series of CT scans while keeping the couch stationary [58]. When the necessary number of images is acquired, the couch is moved to an abutting position and another set of images is acquired. During the process, a breathing surrogate is being monitored and recorded. Fig. 2–1 shows an example of the reconstruction technique used by Low et al. [58]. The process associates a tidal volume with each scan. If the investigator wants to reconstruct a CT image at a specific tidal volume, they query the CT dataset at each couch position and select the CT slices acquired at the tidal volume closest to the desired volume. The accuracy of this method (the difference between the desired and actual tidal volumes) will depend on the reproducibility of the patient's breathing pattern.

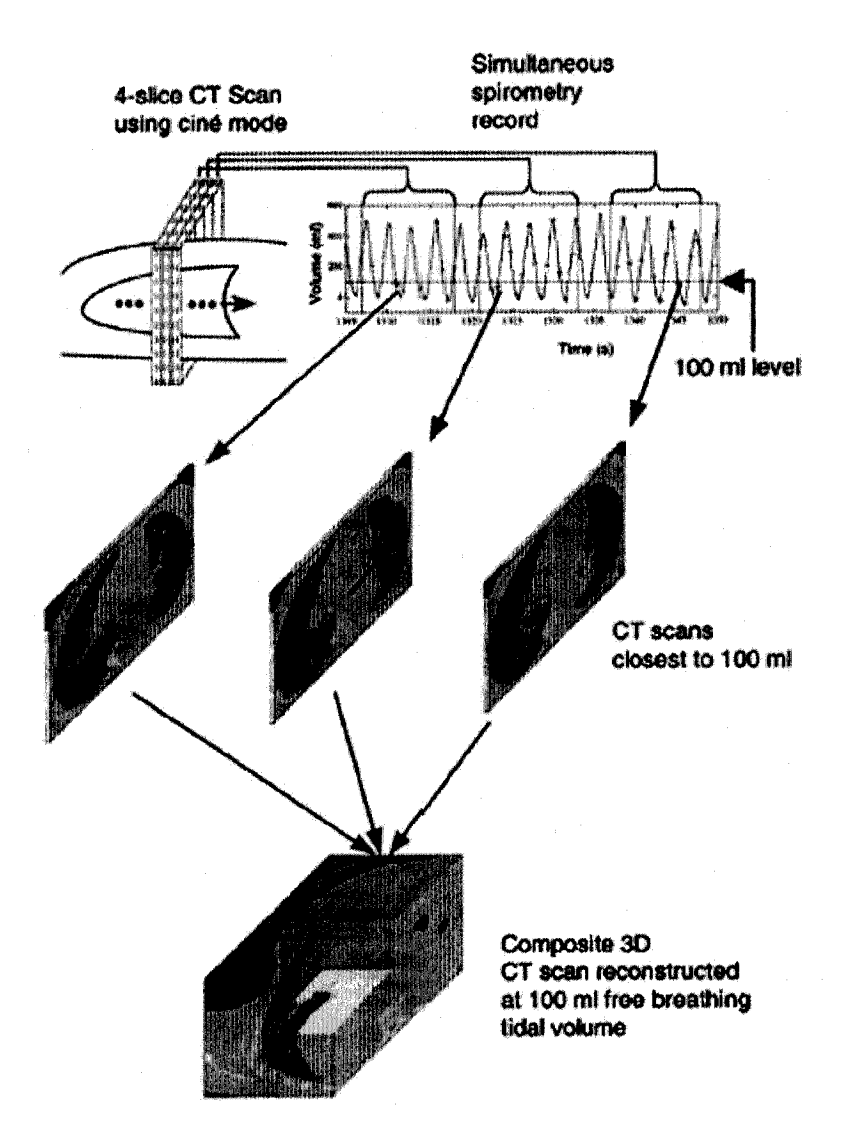


Figure 2–1: Process for breathing amplitude sorting 4D CT scans. The scans are acquired using ciné acquisition while the patient undergoes quantitative spirometry-based breathing monitoring. When a 3D CT scan is required at a particular breathing phase, the breathing trace is queried to determine which scans were acquired at the closest phase to the desired phase and those images are used in subsequent 3D reconstruction. Reproduced from [58].

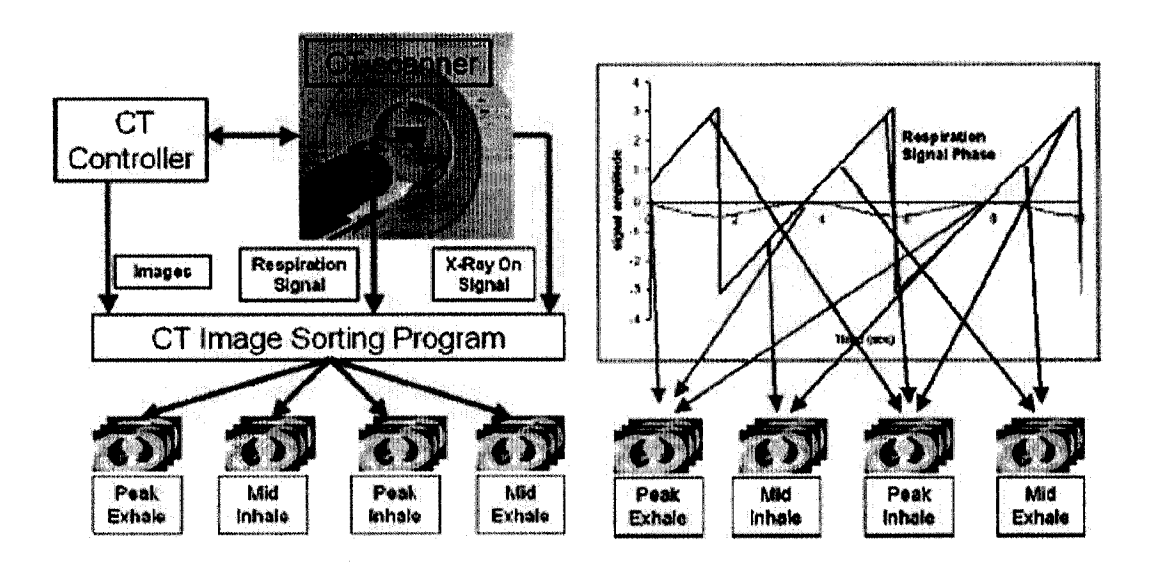


Figure 2–2: The 4D CT phase-sorting process: the CT images, breathing tracking signal and 'X-Ray ON' signal form the input data stream. The breathing cycle is divided into distinct bins (for example, peak exhale, mid inhale, peak inhale, mid exhale). Images are sorted into these image bins depending on the phase of the breathing cycle in which they were acquired, yielding a 4D CT dataset. Reproduced from [110].

Most manufacturer-defined processes use *helical* CT acquisition for 4D CT [23, 47, 62]. This is, in part, due to the fact that they have modified existing cardiac gating software for pulmonary gating, and in part because it is tried to use every available acquired CT projection through the patient. Similar to 4D CT ciné acquisition, a breathing surrogate is simultaneously monitored during the helical CT scanning procedure. When the scan is completed, the user selects one or more breathing phases at which the 3D anatomy needs to be reconstructed. The system will then select all projections acquired at these specified phases and reconstruct a 3D volume for each of them (Fig. 2–2).

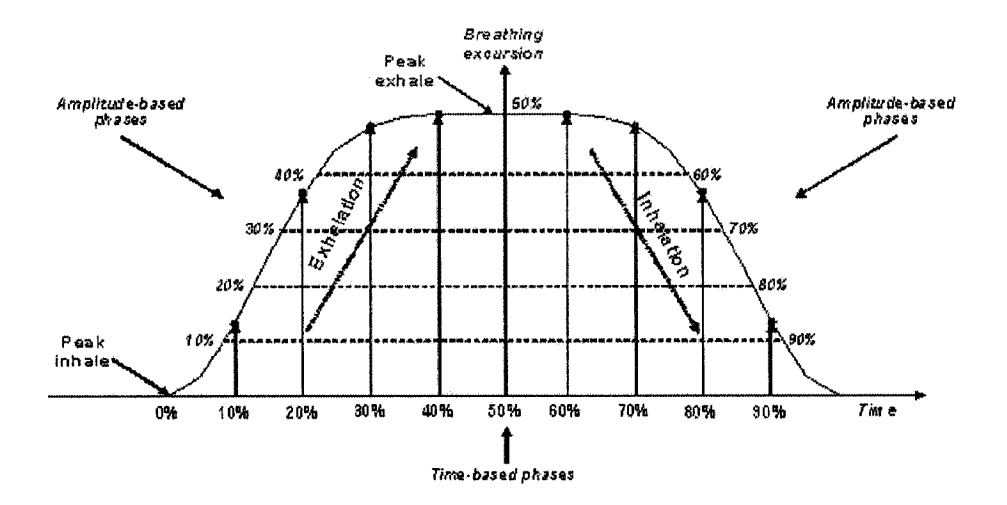


Figure 2–3: Phase labeling in 4D: (a) by time - breathing period is divided into equal intervals and a phase that represents a percentage of the breathing period is assigned to each time interval; (b) by amplitude - breathing excursion is divided into equal intervals and a phase that represents a percentage of the breathing amplitude is assigned to each amplitude interval. Reproduced from [92].

Reconstruction Methods: After CT image acquisition completion, CT slices are typically sorted into different respiratory phases based on either the *amplitude* or the *phase angle* of a respiratory trace (Fig. 2–3).

Because much of the commercial respiratory gating software was adopted from cardiac software, breathing cycles have been defined as though they are reproducible from breath to breath. Phase angles are assigned to the breathing cycle, and a specific and easily identifiable phase is used to define what is meant by 0 degree (e.g., Peak Exhale, see Fig. 2-4) [98, 111]. For example, at a selected point in time, the phase angle is the ratio of the time to the previous 0-degree phase to the time between successive 0-degree phases, normalized to 360 degrees or 2π . However, unlike cardiac motion, breathing is irregular, so each breath can have a different

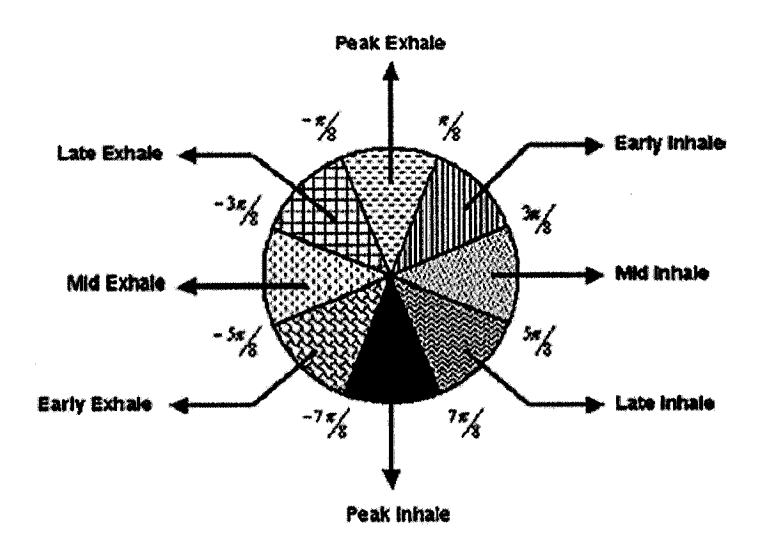


Figure 2–4: Phase-based gating uses a circular description of the breathing cycle. This can be represented by equating each phase of breathing with an angle range. Here, each phase is divided into 45 bins. Reproduced from [111].

depth, residual tidal volume, and frequency. When the breathing frequency is not stable, the phase-based gating approach can still be used because the length of each breath is scaled by the fact that the gating is done as a function of the relative time between the 0-degree phase and the phase of interest. However, amplitude variation is not taken into account and therefore residual motion artifacts can still be present in the reconstructed 4D CT images. Fig. 2–2 shows an example of 4D CT phase-sorting process.

Another approach for gating CT scans is to use amplitude-based gating (Fig. 2–1). The amplitude in this case refers to the magnitude of the respiratory trace. For example, if the Varian's RPM Respiratory Gating System is used, the amplitude would be the relative height of the reflective marker block while for spirometry-based systems, the amplitude is defined by the magnitude of the tidal volume. The CT

slices are segregated according to the depth of breathing and therefore, amplitude variations can be explicitly considered when selecting the appropriate CT scans or projections to reconstruct 3D CT slices at the user-specified breathing phase.

Fig. 2–5 illustrates a comparison between amplitude and phase-angle sorting for a CT acquisition where the peak to peak tidal volume varies appreciably among breaths. Data points from shallow breaths are excluded by amplitude sorting for End Inhale (EI) (Fig. 2–5(c)) but are classified as EI by phase-angle sorting (Fig. 2–5(d)). Basically, phase-angle sorting regards a shallow breath (300 ml) the same as a normal (700 ml) and a deep breath (1000 ml). Clearly, the variation in tidal volume for either respiratory phase is smaller with amplitude sorting than with phase-angle sorting. The amplitude sorting is better than phase angle sorting because the amplitude is more accurately related to target position resulting in reduced residual motion artifacts in a 4D CT dataset. An advantage of phase-angle sorting is that a complete phase angle range (0°-360°) is completely covered with each respiratory cycle; therefore the time for data acquisition is reduced to only one respiratory cycle at each couch position. Breathing coaching is usually considered an important component for 4D CT techniques when phase-angle sorting is used.

To summarize, there are two main goals of 4D CT imaging. First is the accurate imaging of the tumour and normal organ shapes. The interaction of the conventional CT image acquisition sequence and breathing motion causes objects to be imaged with distorted shapes. 4D CT significantly reduces motion artifacts and provides multiple temporally coherent CT volumes during normal respiration (Fig. 2–6). Residual motion artifacts may remain due to partial projection effects.

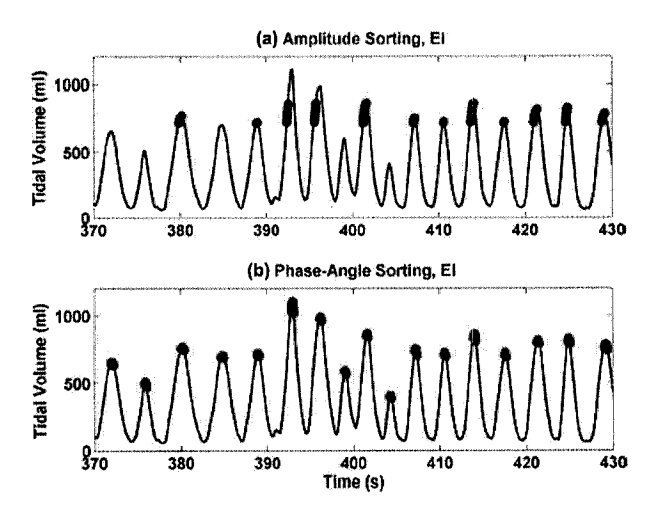


Figure 2–5: Variation in tidal volume with amplitude sorting (a) and phase-angle sorting (b) for the end inhale phase (EI). Thicker segments indicate aggregated data points falling into each respiratory phase. Reproduced from [60].

Temporal coherence within resorted 4D CT volumes is dominated by the number of reconstructed images per slice: the more images are reconstructed, the smaller phase tolerances can be imposed on retrospective sorting.

The second goal of 4D CT imaging is to quantify the motion of the tumour and normal organs. 4D CT data provide the primary image data needed to explicitly include patient-specific respiratory motion into treatment planning in order to ensure dose coverage of the target throughout the breathing cycle and to calculate the dose distributions for the targets and organs at risk when respiratory motion is present during beam delivery.

2.2 4D Treatment planning

The philosophy of designing 4D treatment plans is similar to the one employed in 3D planning in the sense that the overall goal is to maximize the therapeutic ratio

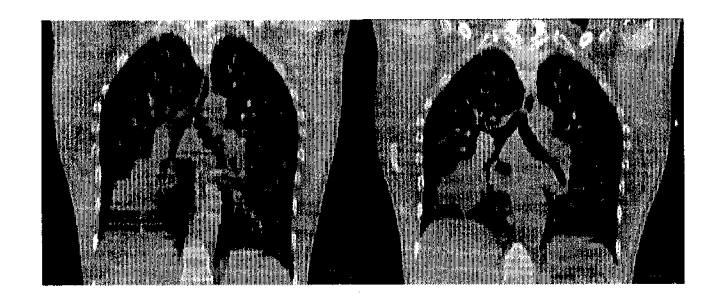


Figure 2–6: Coronal views of CT scans of the same patient taken (a) during free breathing (FB) and (b) with respiratory gated scanning at peak exhale. Reproduced from [45].

by delivering as much dose as possible to the tumour, while sparing normal tissues and organs at risk [26]. However, while the assessment of the dose to be delivered in 4D is still performed on a single dataset, often called the Planning Dataset (PD), the dose reported now represents an accumulation of the doses received during the various phases of the breathing cycle.

The question then is how one could make best use of the abundance of time-dependent anatomical information gathered during imaging when designing the treatment plans. The answer depends on whether the same treatment plan or different plans will be delivered at various phases of the breathing cycle. The term "non-adaptive delivery" will be used for the former approach, whereas the latter one will be referred to as "adaptive delivery". The flow of the events during the treatment planning is schematically shown in Fig. 2–7 for both strategies.

In the case of *non-adaptive delivery*, first the target and other structures of interest are defined on the chosen PD. Then a plan is designed on the PD and dose distributions are re-computed on several datasets at various phases in the breathing cycle using this plan. The last step is the accumulation of these doses and scoring

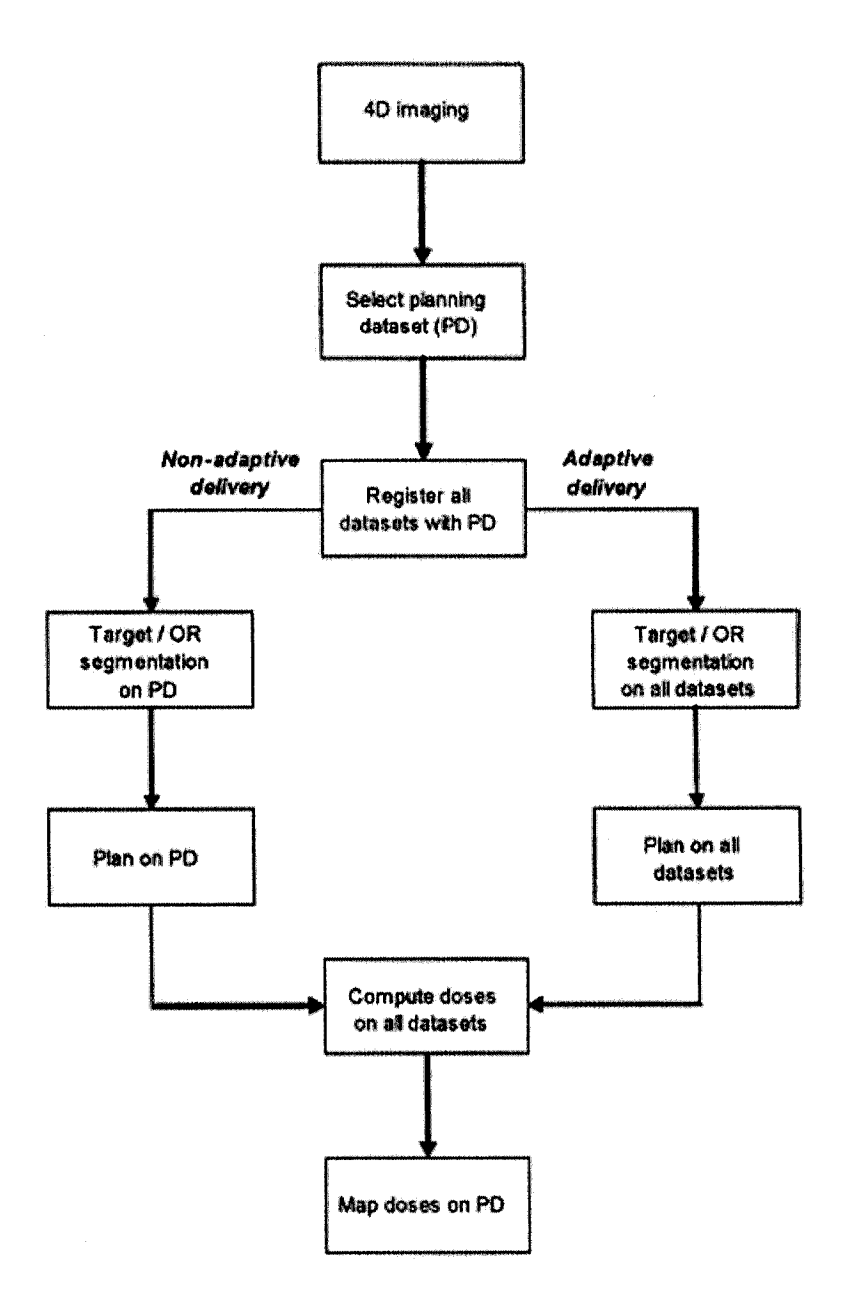


Figure 2–7: The flow of the events during the planning segment of a radiation therapy treatment when 4D imaging data are available (OR = organs at risk). Reproduced from [93].

them back on the PD [35, 46, 96, 84]. The dose accumulation is accomplished by using image registration techniques (discussed in *Chapter 3*) that provide non-rigid body voxel mapping between datasets acquired over various segments of the respiratory cycle [48, 94]. The beam number, weights, and directions are then manipulated until the cumulative dose provides the desired target coverage and normal tissue sparing. This approach is technically 4D only during the imaging segment. However, it is superior to a purely 3D planning because it estimates with increased accuracy the doses that will actually be received by tumor and normal tissues during free breathing delivery.

In a more sophisticated approach, separate plans can be designed on each available dataset with the intent of achieving the desired target coverage at each breathing phase. This implies that the target and other structures of interest have to be first segmented on all datasets. This can be done either manually or automatically *i.e.*, the structures of interest are first segmented on the PD and then mapped on all other datasets using the transformation provided by the registration technique [2, 49, 67, 108]. The treatment beams are added first on the PD and while their directions are kept the same for all datasets, the weights are adjusted and the apertures are modified so that they conform to the target from the beam's eye view for each dataset [42]. Such a treatment planning strategy is followed by an adaptive delivery, in which each plan is delivered when the patient is at the corresponding breathing phase, thus making the entire process (*i.e.*, imaging, planning, and delivery) 4D. Of course, the whole process is subject to the constraints imposed by the ability of the treatment machine to deliver a continually adapting plan. Regardless of the strategy

adopted, the accumulation of the doses on the PD is one common segment achieved using the image registration technique (see *Chapter 3*).

2.3 4D Treatment delivery

A method to allow margin reduction without compromising tumour dose is to allow the patient to breath freely while a tracking-and-control system monitors the tumour's position and continuously adapts the alignment of the radiation field to follow the moving target. The goal is to adapt treatment planning and delivery to the changes caused by respiration in the entire anatomy. 4D treatment delivery has the advantage of allowing the beam to be 'ON' continuously. Thus there is virtually no increase in delivery time as opposed to beam gating or breath hold techniques.

In essence, the 4D motion adaptive delivery is a superposition of the target motion upon the original beam planned for delivery (Fig. 2–8). While in motion adaptive delivery beam-view, the target is static, in the conventional beam-view, the target appears smeared out, and thus a larger field is needed to cover the target (Fig. 2–9).

There are presently two real-time beam-positioning methods. The first one is MLC repositioning [73, 76, 77, 104, 113, 114]. The second method uses a robotic manipulator to move the entire linear accelerator with six degrees of freedom. In this approach, the robot (CyberKnife image-guided radiosurgery system) is coupled through a real-time control loop to an imaging system that monitors the tumour position and directs the repositioning of the linear accelerator [10, 70, 75, 97] and has the advantage of adapting to the full 3D motion of the tumour.

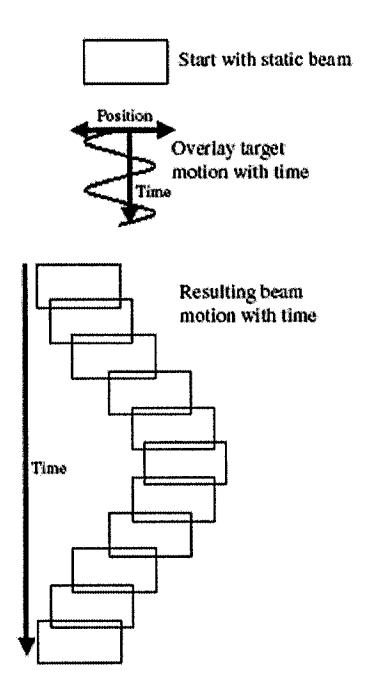


Figure 2–8: A schematic diagram of the superposition of the target motion upon the beam planned for treatment. Reproduced from [44].

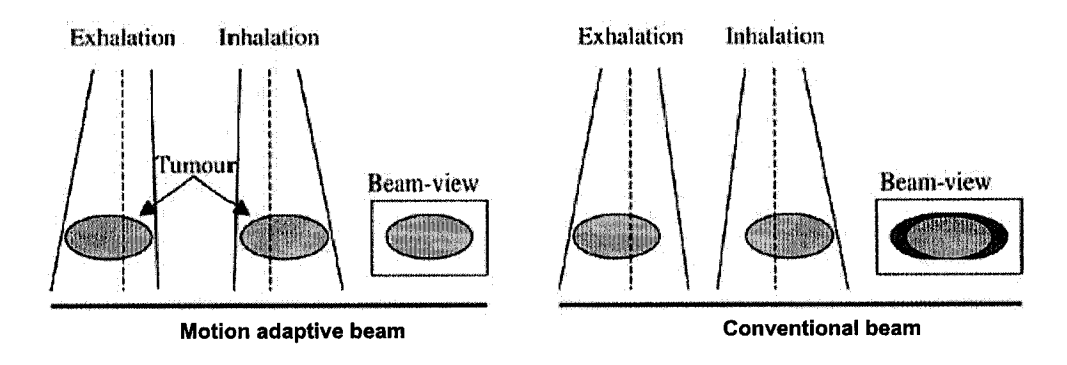


Figure 2–9: Diagram showing the moving target remaining static in the adaptive delivery. The conventional plan with a static beam and increased margins is shown for comparison. Reproduced from [44].

CHAPTER 3 Image Registration Techniques

Radiological images are increasingly being used in healthcare and medical research. There is, consequently, widespread interest in accurately relating information in the different images for diagnosis, treatment and basic science. Applications of image registration include combining images of the same subject from different modalities, aligning temporal sequences of images to compensate for motion of the subject between scans, image guidance during interventions and aligning images from multiple subjects in cohort studies. Current registration algorithms can, in many cases, automatically register images that are related by a rigid body transformation (i.e., where tissue deformation can be ignored). There has also been substantial progress in non-rigid registration algorithms that can compensate for tissue deformation, or align images from different subjects. Nevertheless many registration problems remain unsolved, and this is likely to continue to be an active field of research in the future.

This chapter reviews registration techniques used to solve this problem, and describes the Automated Nonlinear Image Matching and Anatomical Labeling (AN-IMAL) non-linear registration algorithm used for the image registration of the deformable lung phantom and presented in *Chapter 5*.

3.1 Classification of registration methods

Image registration is a process for determining the correspondence of features between images collected at different times or using different imaging modalities. The correspondences can be used to change the appearance - by rotating, translating, stretching, etc - of one image so it more closely resembles another so the pair can be directly compared, combined or analysed (Fig. 3–1).

Since information gained from two imaging modalities is usually of a complementary nature, proper integration of useful data obtained from the separate images is often desired. A first step in this integration process is to bring the modalities involved into spatial alignment, a procedure referred to as *registration*. After registration, a *fusion* step is required for the integrated display of the data involved [63, 107, 78].

Image registration methods can be classified based on the following criteria: (1) modalities involved; (2) subject; (3) type of transformation; and (4) interaction.

1. Modalities involved: monomodal and multimodal

Medical imaging modalities can be divided into two major categories: anatomical and functional modalities. Anatomical modalities, i.e., depicting primarily morphology, include X-ray, computed tomography (CT), magnetic resonance imaging (MRI), ultrasound (US), portal images, and (video) sequences obtained by various catheter "scopes", e.g., by laparoscopy or laryngoscopy. Functional modalities, i.e., depicting primarily information on the metabolism of the underlying anatomy, include (planar) scintigraphy, single photon emission computed tomography (SPECT), positron

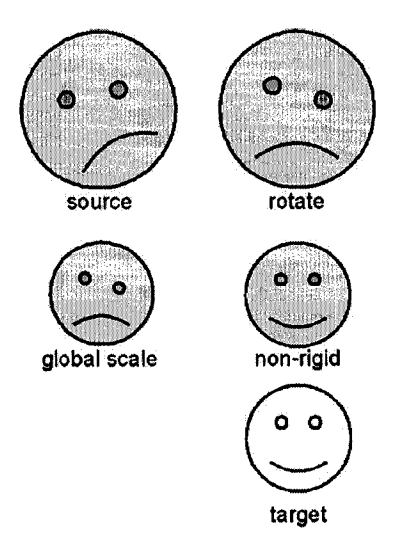


Figure 3–1: Schematic showing rigid and non-rigid registration. The source image is rotated, of a different size and contains different internal structure to the target. These differences are corrected by a series of steps with the global changes generally being determined before the local changes. Reproduced from [107]

emission tomography (PET), which together make up the nuclear medicine imaging modalities, and functional MRI (fMRI).

In monomodal applications, the images to be registered belong to the same modality, and therefore images showing different aspects of tissue morphology are combined. In multimodal registration tasks, where the images to be registered stem from two different modalities, tissue metabolism and its spatial location relative to anatomical structures are related.

2. Subject: intrasubject, intersubject and atlas.

When all of the images involved in a registration task are acquired on a single patient, we refer to it as *intrasubject* registration. If the registration is accomplished

using two images of different patients (or a patient and a model), this is referred to as *intersubject* registration. If one image is acquired from a single patient, and the other image is somehow constructed from an image information database obtained using imaging of many subjects, we name it *atlas* registration.

3. Type of transformation: rigid, affine and non-rigid

The rigid methods can be used to cope with rotation and translation differences between the registered images. Today rigid registration is often extended to include affine registration, which includes scale factors and shears, and can partially correct for calibration differences across scanners or gross differences in scale between subjects. Specific problems arise due to differences in patient posture for different studies, possible differences in organ shape and volume (e.g., stomach and bladder content), so non-rigid methods are required to cope with local differences between the images. Rigid and affine transformations are commonly used as a first estimate before determining a non-rigid transformation.

4. Interaction: interactive, semi-automatic and automatic.

Concerning registration algorithms, three levels of interaction can be recognized.

Automatic, where the user only supplies the algorithm with the image data and possibly information on the image acquisition. Interactive, where the user does the registration himself, assisted by software supplying a visual or numerical impression of the current transformation, and possibly an initial transformation guess. Semi-automatic, where the interaction required can be of two different natures: the user

needs to initialize the algorithm, (e.g., by segmenting the data), or steer the algorithm, (e.g., by selecting homologous landmarks in both images). The points selected to create homologous sets are those that serve as anatomical landmarks and usually have biologically meaningful labels. These landmarks must be defined with respect to their local neighbourhood, i.e., the point of contact between two structures, a point of extreme curvature of a surface or the center of a structure. The anatomical landmark and segmentation-based methods are commonly semi-automatic (user initializing), and the voxel property based methods are usually automated.

3.2 Applications of image registration

An eminent example of the use of registering different modalities can be found in the area of radiotherapy treatment, where both CT and MR can be employed. The former is needed to accurately compute the radiation dose, while the latter is usually better suited for delineation of tumour tissue.

Besides multimodality registration, important applications exist in monomodality registration. Examples include treatment verification by comparison of pre- and post-intervention images, comparison of ictal and inter-ictal (during and between seizures) SPECT images, and growth monitoring (e.g., using time series of MR scans on tumors, or X-ray time series on specific bones).

There is growing interest in applying registration to organs subject to motion and non-rigid deformation often with a view to tracking their position and shape during breathing to allow delivery of targeted treatments for cancer such as external beam radiotherapy or thermal/cryo ablation [6, 103]. This often involves registration of planning images acquired pre-treatment, possibly on a different day at a different site, with images acquired during treatment. For some organs there will be gross deformations owing to patient positioning as well as differences owing to different stomach, bowel and bladder contents, and owing to breathing. Lung deformation during the breathing cycle is also of interest, especially for external beam radiotherapy applications [27, 66].

Central to the use of registration in radiotherapy is to calculate effective dose distributions in the presence of motion, where different respiratory states must be deformably registered to a reference volume to track dose delivered to individual voxels. Moreover, the non-linear registration between 4D CT image datasets can be used to map contours from the reference state to each phase, allowing for automatic contouring/segmentation.

3.3 Image registration in theory

3.3.1 Components of an image registration algorithm

Registration is the determination of a one-to-one transformation between two image spaces which maps each point of an image onto corresponding points of another image. The registration algorithm can be decomposed into three components:

- 1. The *similarity metric* defines features to match between source and target images and quantifies image matching.
- 2. The transformation model specifies the way in which the source image can be changed to match the target. A number of numerical parameters specify a particular instance of the transformation.
- 3. The optimization method varies the parameters of the transformation model to maximize the similarity metric.

1. Similarity measures

There are two approaches to registration based on patient image content: the geometric approach and the intensity approach [88]

Geometric approaches build explicit models of identifiable anatomical elements in each image. They minimize the distance between features such as points (land-marks), curves or surfaces of corresponding anatomical structures and require the identification and matching of these features on both reference and test images. This process usually needs a certain amount of human interaction. After point matching, the remaining procedure of registration is only interpolation or approximation.

Intensity approaches match intensity patterns in each image using mathematical or statistical criteria. They define a measure of intensity similarity between the source and the target and adjust the transformation until the similarity measure is maximized. Measures of similarity include squared differences in intensities, correlation coefficient, measures based on optical flow and information-theoretic measures such as mutual information [61, 81, 103]. All these measures are defined formally in Table 3–1.

The simplest similarity measure is the sum of squared differences, which assumes that the images are identical at registration except for (Gaussian) noise. The correlation coefficient assumes that corresponding intensities in the images have a linear relationship. These two similarity measures are suitable for monomodal registration where the intensity characteristics are very similar in the images. For multimodal registration, similarity measures have been developed, which define weaker relationships between intensities to reflect the different intensity characteristics of different

Table 3–1: Common image similarity measures used in registration. T is the target image, S the source image, T the transformation that maps both position and intensity (i.e., takes account of interpolation and sampling), S^T the image S transformed into the coordinate space of image T, x a point in T image. Reproduced from [107]

Voxel similarity measures	Comment	
Sum of Squared Differences $SSD = \frac{1}{N} \sum_{\mathbf{x}} \left(T(\mathbf{x}) - \mathbf{S}^{T}(\mathbf{x}) \right)^{2}$	Registered images differ only by Gaussian noise. Sensitive to small number of voxels that have very large intensities differences. Only for monomodal image registration.	
$Correlation coefficient \\ CC = \frac{\sum_{\mathbf{x}} (T(\mathbf{x}) - \overline{\mathbf{T}}) \cdot (\mathbf{S}^{T}(\mathbf{x}) - \overline{\mathbf{S}})}{\{\sum_{\mathbf{x}} (T(\mathbf{x}) - \overline{\mathbf{T}})^{2} \cdot \sum_{\mathbf{x}} (\mathbf{S}^{T}(\mathbf{x}) - \overline{\mathbf{S}})^{2}\}^{1/2}}$	Registered images have linear intensity relationship and ob-	
$\{\sum_{\mathbf{x}} (T(\mathbf{x}) - T)^2 \cdot \sum_{\mathbf{x}} (S^2(\mathbf{x}) - S)^2\}^{-7/2}$	jects of interest are in the field of view of both images. Only for monomodal image registration.	
Correlation ratio $\eta = 1 - \frac{1}{N\sigma^2} \sum_i N_i {\sigma_i}^2$	The correlation ratio assumes a functional relationship between intensities. It can be defined in terms of sums of squares of source voxels that correspond to a number N_i of iso-intense voxels in the target image. $\sigma^2 = \frac{1}{N} \sum_{\substack{overlap \mathbf{x} \\ \mathbf{x}: \mathbf{T}(\mathbf{x}) = \mathbf{i}}} S(\mathbf{x})^2 - \mathbf{m}^2, \qquad m = \frac{1}{N} \sum_{\substack{overlap \mathbf{x} \\ \mathbf{x}: \mathbf{T}(\mathbf{x}) = \mathbf{i}}} S(\mathbf{x}),$	
Mutual information $MI = H_T + H_S - H_{TS}$	Defined in terms of entropies of the intensity distribution $H_T = -\sum_i P_i \log P_i$, $H_S = -\sum_j Q_j \log Q_j$, and $H_{TS} = -\sum_{ij} p_{ij} \log p_{ij}$ where $P(Q)$ =probability of intensity $I(J)$ occurring in target (source) and p_{ij} = joint probability of both occurring at the same place.	
Normalized mutual information $NMI = \frac{H_T + H_S}{H_{TS}}$	Proposed to minimize the overlap problem seen occasionally with mutual information	

imaging modalities. The *correlation ratio* [87] assumes that corresponding intensities are functionally related at registration and information-theoretic measures like *mutual information* assume only that a probabilistic relationship between voxel intensities is maximized at registration.

Intensity-based registration match intensity patterns over the whole image but do not use anatomical knowledge. Geometric registration uses anatomical information but usually sparsely distributed throughout the images. Combining geometric features and intensity features in registration should result in more robust methods. Hybrid algorithms are therefore of particular current interest, combining intensity-based and model-based criteria to establish more accurate correspondences in difficult registration problems.

2. Transformation models

The transformation model defines how one image can be deformed to match another image and therefore characterizes the type and number of possible deformations.

The most well known examples are the *rigid* and *affine* transformations that can be described very compactly by 6 (3 translations and 3 rotations) to 12 (3 translations + 3 rotations + 3 scalings + 3 shears) parameters for a whole image. These parameters are applied to a vector locating a point in an image to find its location in another image. The transformation model serves two purposes: first, it controls how image features can be moved relative to one another to improve the image similarity and, second, it interpolates between those features where there is no useable information.

As for the transformations used in non-rigid registration one of the most important is the family of splines. Spline-based registration algorithms use corresponding "control" points, in the source and target image and a spline function to define correspondences away from these points. The "thin-plate" spline [8] has been used extensively to investigate subtle morphometric variation in schizophrenia [15, 16, 30]. Each control point belonging to a thin-plate spline has a global influence on the transformation in that, if its position is perturbed, all other points in the transformed image change. This can be a disadvantage because it limits the ability to model complex and localized deformations and because, as the number of control points increases, the computational cost associated with moving a single point rises steeply. By contrast, B-splines are only defined in the vicinity of each control point and therefore perturbing the position of one control point only affects the transformation in the neighbourhood of the point. Because of this property, B-splines are often referred to as having "local support". B-spline based non-rigid registration techniques are popular due to their general applicability, transparency and computational efficiency. Their main disadvantage is that special measures are sometimes required to prevent folding of the deformation field and these measures become more difficult to enforce at finer resolutions.

Elastic models treat the source image as a linear, elastic solid [3] and deform it using forces derived from an image similarity measure. The elastic model results in an internal force that opposes the external image matching force. The image is deformed until the forces reach equilibrium. Since the linear elasticity assumption is only valid for small deformations it is hard to recover large image differences

with these techniques. Replacing the elastic model by a viscous fluid model [12] allows large and highly localized deformations. The higher flexibility increases the opportunity for misregistration, generally involving the growth of one region instead of shifting or distorting another [55].

Finite element (FE) models allow more control of localized deformations and have been applied particularly to the head surgery [22, 32]. These models divide the image into cells and assign to these cells a local physical description of the anatomical structure. For instance, soft tissue can be labeled as elastic, bone as rigid and cerebrospinal fluid (CSF) as fluid. External forces such as landmark correspondences or voxel similarity measures are applied to the model, which deforms according to the material behaviour in each cell. Such approaches tend to be used where there are strong biomechanical constraints in operation, i.e., they are appropriate for serial registration of images of brains undergoing some mechanical intervention but not appropriate for intersubject registration.

3. Optimization method

Optimization refers to the manner in which the transformation is adjusted to improve the image similarity. A good optimizer is one that reliably and quickly finds the best possible transformation. Most of the registration algorithms require an iterative approach, in which an initial estimate of the transformation is gradually refined by trial and error. In each iteration, the current estimate of the transformation is used to calculate a similarity measure. The optimization algorithm then makes another (hopefully better) estimate of the transformation, evaluates the similarity measure again, and continues until the algorithm converges, at which point no

transformation can be found that results in a better value of the similarity measure, to within a preset tolerance.

3.3.2 Validation of image registration

Validation usually means showing that a registration algorithm applied to typical data in a given application consistently succeeds with a maximum (or average) error acceptable for the application.

Quantification of the accuracy of DIR is challenging, because the ground truth is difficult to establish for patient data and phantoms, which exhibit that the complex deformations of the human body are difficult to manufacture. The accuracy of DIR has been reported using both qualitative and quantitative metrics. Qualitative assessment of DIR accuracy includes visual examination of difference images and image overlays [65]. In most applications, careful visual inspection remains the first and most important validation check.

Quantitative metrics include a comparison of the predicted and actual displacement of landmarks identified on two images, comparison with a known deformation field, consistency testing, similarity metrics of image intensity and distance-to-agreement (DTA) of 3D surfaces derived from contoured planning structures.

One common approach is to identify corresponding landmarks or regions independently of the registration process and establish how well the registration brings them into alignment [13, 34, 65, 85, 116]. Readily identifiable anatomical features such as vessel and bronchial bifurcations and intersections, bony anatomy may be used to evaluate a distance metric of the accuracy of the registration. This method is limited by the accuracy with which corresponding landmarks can be identified.

Another method to evaluate the registration accuracy is by comparison with a known deformation field [112]. The image is deformed with a known deformation field (mathematical or derived from registration with another model) and the estimated deformation is subsequently compared with the "true" deformation. To make this a realistic test, deformations that simulate most closely the type of deformations that occur in the anatomy to register should be used.

Various kinds of consistency tests are also used in validation; the most common are establishing that registration of source to target produces the same alignment as from target to source (this is commonly not the case for non-rigid registration) or that for three images, A, B, C, registration of $C \to A$ gives the same result as $C \to B$ compounded with $B \to A$ [11, 37, 117].

Similarity metrics of image intensity are also used, by comparing the correlation of image intensities between the transformed source image by the recovered deformation field and the target image [34].

For the distance-to-agreement (DTA) of 3D surfaces method, a 3D average DTA is calculated by averaging the minimum distances between the deformed source and target 3D surfaces for each triangle of the deformed surface along its normal [34].

3.4 The ANIMAL non-linear registration algorithm

This section describes a completely automatic method to register a given volumetric dataset to another, based on a linear-elastic model of tissue deformation, an intensity based similarity function equal to a correlation coefficient and a non-linear simplex optimizer. The ANIMAL algorithm is applicable to both intra- and intersubject intra-modality registration and uses automatic feature-matching, obviating

the need for user intervention (landmark tagging) as in the case of semi-automatic registration methods. Registration of the model with the source volume is accomplished in two optimization steps: the first accounts for the linear component of the transformation function, and the second for the non-linear component. Once found, the transformation can be used to resample the first dataset in the coordinate space of the second, thus aligning them geometrically so that corresponding morphological features of both data sets are assigned to the same spatial location.

3.4.1 Feature detection

Both linear and non-linear registration procedures begin by extracting salient features from the image data that will be used in the evaluation of the matching process. For this purpose the blurred image intensity and image gradient magnitude are used, so that the value of a feature corresponding to a particular anatomical landmark is the same, regardless of its position or orientation within the image volume. These features are calculated by convolution of the original data with zeroth and first order 3D isotropic Gaussian derivatives (Fig. 3–2). Convolution with such an operator maintains linearity, shift-invariance and rotational-invariance in the detection of features [13]. The Gaussian kernel has a scalable property since it is dependent on the standard deviation, σ . The full-width-half-max (FWHM = 2.35 σ) of this kernel is used as parameter to measure the spatial scale. This parameter must be chosen carefully in relation to the scale of the estimated deformation function. A very large value will introduce too much blurring, possibly removing important structural detail. Too small a value will extract a lot of structures and consequently increase the probability of local mis-matches. The size of the Gaussian blurring

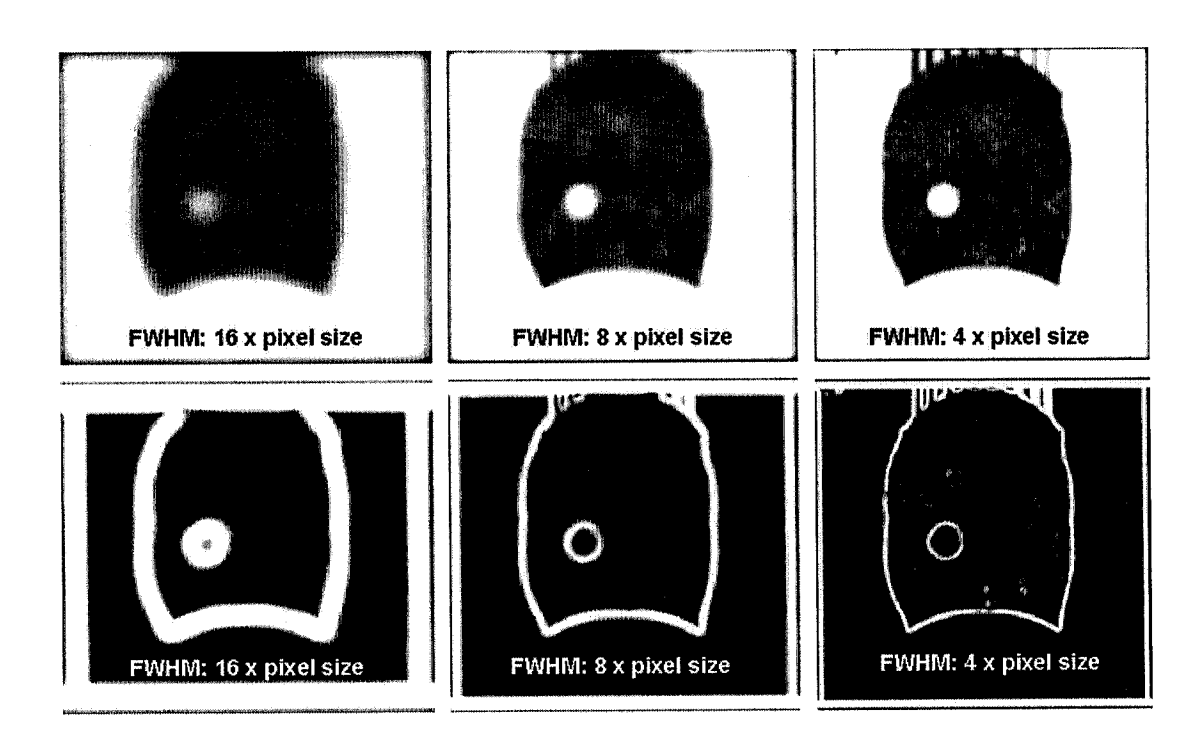


Figure 3–2: Computed tomography sagittal cuts through the volumetric features of four data states at scales of FWHM=16, 8, 4 mm. The top row shows a sagittal cut through the original data. The middle row shows the same slice blurred with a 3D Gaussian kernel with FWHM=16, 8, 4 mm. The last row shows the corresponding gradient magnitude data at the same scale.

kernel applied to the volumetric data was chosen to be equal to the resolution of the deformation field estimated at the current scale step.

3.4.2 Transformation model

Linear registration: Linear transformations for volumetric registration are either rigid or affine, where the former is a subset of the latter. A rigid transformation can be decomposed into a translation component to center one data set on the other and

a rotation component to align their orientations. The affine transformation can be decomposed into translation and rotation as before, with the addition of scaling and shearing.

Using matrix formulation and homogeneous coordinates, a point (x, y, z, 1) is mapped to the point (x', y', z', 1) using a homogeneous coordinate transformation:

$$(x', y', z', 1) = [\mathbf{A}](x, y, z, 1)', \tag{3.1}$$

where **A** is a 4x4 affine transformation matrix containing 12 independent elements and results from the concatenation of 4 matrices, representing translation, rotation, scaling and shear:

$$\mathbf{A} = [\mathbf{Sh}][\mathbf{Sc}][\mathbf{R}][\mathbf{T}]. \tag{3.2}$$

The matrices T, R, Sc, Sh are defined as follows:

$$\mathbf{T} = \begin{bmatrix} 1 & 0 & 0 & tx \\ 0 & 1 & 0 & ty \\ 0 & 0 & 1 & tz \\ 0 & 0 & 0 & 1 \end{bmatrix}, \tag{3.3}$$

where tx, ty and tz are the translations in x, y and z between the centroid of the two volumes.

$$\mathbf{R} = [\Theta][\Phi][\Psi],\tag{3.4}$$

where

$$\Theta = \begin{bmatrix} 1 & 0 & 0 & 0 \\ 0 & \cos\theta & \sin\theta & 0 \\ 0 & -\sin\theta & \cos\theta & 0 \\ 0 & 0 & 0 & 1 \end{bmatrix},$$
(3.5)

$$\Phi = \begin{bmatrix}
\cos\phi & 0 & -\sin\phi & 0 \\
0 & 1 & 0 & 0 \\
\sin\phi & 0 & \cos\phi & 0 \\
0 & 0 & 0 & 1
\end{bmatrix},$$
(3.6)

$$\Psi = \begin{bmatrix} \cos\psi & \sin\psi & 0 & 0 \\ -\sin\psi & \cos\psi & 0 & 0 \\ 0 & 0 & 1 & 0 \\ 0 & 0 & 0 & 1 \end{bmatrix}.$$
 (3.7)

The angles θ , ϕ and ψ are clockwise rotations around the $x,\ y$ and z axes, respectively.

$$\mathbf{Sc} = \begin{bmatrix} sx & 0 & 0 & 0 \\ 0 & sy & 0 & 0 \\ 0 & 0 & sz & 0 \\ 0 & 0 & 0 & 1 \end{bmatrix}, \tag{3.8}$$

where sx, sy and sz are scaling factors along each of the axes.

$$\mathbf{Sh} = \begin{bmatrix} 1 & 0 & 0 & 0 \\ a & 1 & 0 & 0 \\ b & c & 1 & 0 \\ 0 & 0 & 0 & 1 \end{bmatrix},\tag{3.9}$$

where a, b and c are the three free parameters left to define the shear matrix \mathbf{Sh} . The shear parameters convert a rectangular parallelepiped into an oblique one.

Non-linear registration: The goal of the ANIMAL algorithm is to recover the nonlinear transformation N required to register the source and target volumes. In the implementation of the algorithm, N is represented by a deformation field that is defined on an isotropic 3D cubic lattice, \mathcal{L} , with a 3D displacement vector stored for each node position in the lattice (Fig. 3–3). In practice, three scalar values are stored (dx, dy, dz), representing the x, y and z components of the 3D displacement vectors. For a given arbitrary (x, y, z) position in the domain of the deformation function, the value of the corresponding 3D displacement is given by interpolation in each component volume, yielding the three necessary values for the 3D vector. If the FWHM of the current scale step is used to measure resolution, then the voxel spacing of the deformation field lattice must be no greater than FWHM/2 to recover the function without aliasing, i.e., the usual Nyquist sampling limit (Fig. 3–4).

3.4.3 Similarity measures

Linear Registration. Correlation is used as a measure of goodness-of-fit between the transformed volume and the target volume. At a given scale step, the correlation value is evaluated on a set of voxel positions, \mathcal{L} , organized on a 3D cubic lattice, with

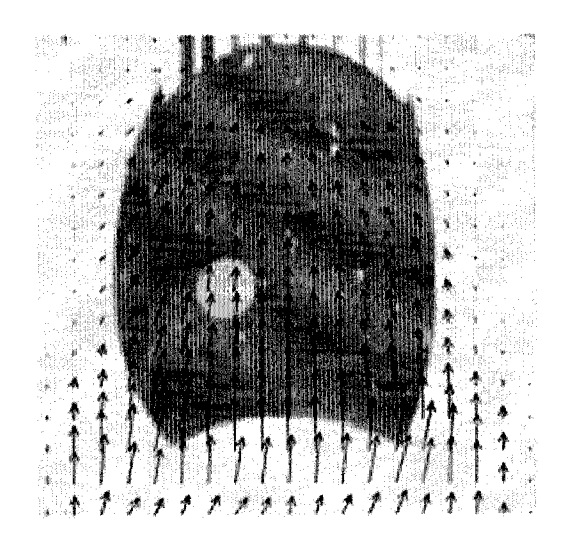


Figure 3–3: Deformation field N defined on an isotropic cubic lattice, with a 3D displacement vector stored for each position in the lattice.

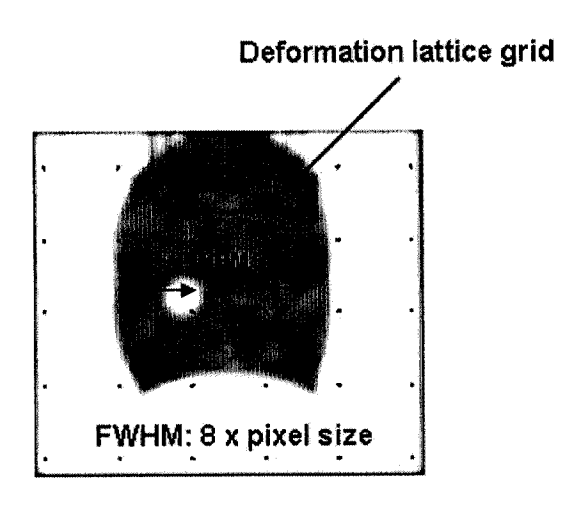


Figure 3–4: 3D isotropic deformation lattice grid overlaid on the blurred image intensity data. The FWHM of the isotropic Gaussian kernel is used to measure the image resolution. The lattice spacing equals half of the FWHM distance of the current scale.

spacing between each lattice point equal to half of the FWHM distance of the current scale. Let \vec{x} be an element of \mathcal{L} . The points used to calculate the cross-correlation are those within the source volume (S) and that map through \mathbf{A} into unmasked voxels in the target volume (T); *i.e.*,

$$\mathcal{L} = \{ \vec{x} \mid \forall \vec{x}, \vec{x} \in \mathcal{S} \land \mathbf{A} \cdot \vec{x} \in \mathcal{T} \}$$
 (3.10)

The normalized cross-correlation value, R(), between the two volumes, S and T for a given transformation A is defined as:

$$R\left(\mathcal{S}, \mathcal{T}; \mathbf{A}\right) = \frac{\sum_{\vec{x} \in \mathcal{L}} f\left(\mathcal{S}, \vec{x}\right) f\left(\mathcal{T}, \mathbf{A} \cdot \vec{x}\right)}{\left(\sum_{\vec{x} \in \mathcal{L}} f^{2}\left(\mathcal{S}, \vec{x}\right)\right)^{1/2} \left(\sum_{\vec{x} \in \mathcal{L}} f^{2}\left(\mathcal{T}, \mathbf{A} \cdot \vec{x}\right)\right)^{1/2}}$$
(3.11)

where f() is the interpolated feature value from the volume S or T at the voxel position \vec{x} , and the summation is done over all elements $\vec{x} \in \mathcal{L}$. R takes on a maximum value of 1.0 when the two volumes are in perfect registration. In the registration algorithm, this function is evaluated at each step of the optimization procedure described in the following section.

Non-linear Registration. The deformation is recovered by estimating the necessary local deformation at each node of \mathcal{L} that minimizes an objective function (Eq. 3.12) consisting of an image local similarity function $R(\mathcal{S}, \mathcal{T}; \mathbf{N}, \vec{x})$ (i.e., local correlation coefficient) and a cost function $C(\mathbf{N}, \vec{x})$ (linear-elastic) properly weighted to obtain the desired level of deformation smoothness.

$$S(\mathcal{S}, \mathcal{T}; \mathbf{N}) = \frac{1}{n} \sum_{\vec{x} \in \mathcal{L}} [\alpha R(\mathcal{S}, \mathcal{T}; \mathbf{N}, \vec{x}) + (1 - \alpha)C(\mathbf{N}, \vec{x})],$$
(3.12)

where S and T are the source and target volumes; N is the non-linear transformation represented by the deformation field that maps points from S to T; R() is the local similarity measure; C() is the cost function and α is the similarity to cost ratio, $0 \le \alpha \le 1.0$. The summation is evaluated over all nodes, \vec{x} , in the 3D lattice, \mathcal{L} , of the deformation field, and is normalized by the number of nodes, n.

The image similarity function is based on maximizing the correlation coefficient given by Eq. 3.13. The correlation coefficient is estimated at each of the lattice nodes using the same principle as the linear registration; however, the correlation is based on a summation over a set of voxels in the local neighbourhood of the particular node. Hence, R() is the normalized correlation value between the local neighbourhood of \vec{x} in the source volume S and the corresponding neighbourhood of $N(\vec{x})$ in the target volume T.

$$R\left(\mathcal{S}, \mathcal{T}; \mathbf{N}, \vec{x}\right) = \frac{\sum_{v \in \mathcal{N}_{\vec{x}}} f\left(\mathcal{S}, v\right) f\left(\mathcal{T}, \mathbf{N}\left(v\right)\right)}{\left(\sum_{v \in \mathcal{N}_{\vec{x}}} f^{2}\left(\mathcal{S}, v\right)\right)^{1/2} \left(\sum_{v \in \mathcal{N}_{\vec{x}}} f^{2}\left(\mathcal{T}, \mathbf{N}\left(v\right)\right)\right)^{1/2}}$$
(3.13)

where N is the nonlinear transformation represented by the deformation field that maps points from S to T; $\mathcal{N}_{\vec{x}}$ is the local neighbourhood of \vec{x} with diameter 1.5 FWHM, f () is the volumetric interpolation function, and the summation is performed over all voxel elements $v \in \mathcal{N}_{\vec{x}}$. The local neighbourhood of \vec{x} , $\mathcal{N}_{\vec{x}}$, is defined

by a sublattice of nodes v. The sublattice parameter defines the number of nodes within the lattice diameter at which image similarity is measured (i.e. sublattice = 3 specifies that image similarity is measured on a 3 x 3 x 3 grid) and should be chosen such that the node spacing is larger than the image resolution.

The cost function C() penalizes deformations on the order of d_{max} which is the spacing of the deformation lattice nodes (Eq. 3.14).

$$C(\mathbf{N}, \vec{x}) = \begin{cases} \frac{0.2d^{3/2}}{d_{max}^3 - d^{3/2}}, & \text{if } d^{3/2} \le d_{max}^3\\ \infty, & \text{otherwise} \end{cases}$$
(3.14)

3.4.4 Optimization method

Linear Registration: The 3D image registration task is set up as an optimization problem to identify the required transformation while minimizing the computational complexity usually associated with an exhaustive grid search approach. The optimization is performed at different spatial resolutions to minimize the problems associated with local minima in the solution hyper-surface, starting with very blurred data and increasing detail at each step by using less blurred images.

Non-linear Registration: The non-linear registration process can be represented as two nested loops. The *outer loop* iterates over different deformation lattice spacings in a coarse-to-fine manner, while the *inner loop* recovers the optimized deformations at a given deformation lattice spacing.

The first iteration of the outer loop begins with very blurred data (FWHM=16 mm) so that gross image features drive the fit at first. When the optimal solution is obtained for the FWHM=16 mm scale, it is used as a starting point for the same

process calculated with the blurred intensity feature volumes at FWHM=8 mm scale. Image blurring and lattice grid spacing are reduced after each iteration, with each successive step refining the estimation of the previous step. Data blurred to have isotropic resolution of 16, 8, 4, and 2 were used sequantelly to calculate the multiscale registration. The use of the global multi-resolution strategy provides a smoother objective function and a shorter execution time.

At each scale step of the outer loop, the inner loop recovers the deformation vector at each node in an iterative manner by minimizing an objective function which maximizes the correlation coefficient in a local neighbourhood of that node whilst penalizing deformation on the order of the deformation lattice spacing. The local optimization at each node will result in the global optimization of the whole field.

Eq. 3.12 is maximized when each of the terms in the summation are at a maximum. Since the transformation N is stored such that there is one deformation vector for each node \vec{x} , Eq. 3.12 is maximized by optimization at each node of \mathcal{L} .

The optimization is similar to that performed for the linear registration procedure; however, only three parameters are optimized instead of nine, since only three are required to define the local deformation vector \vec{d} that maximizes the correlation of the local neighbourhood of \vec{x} with its homologue in the target volume. Hence, the goal is to find \vec{d} that maximizes $R(\mathcal{S}, \mathcal{T}; (\mathbf{N} + \vec{d}), \vec{x})$.

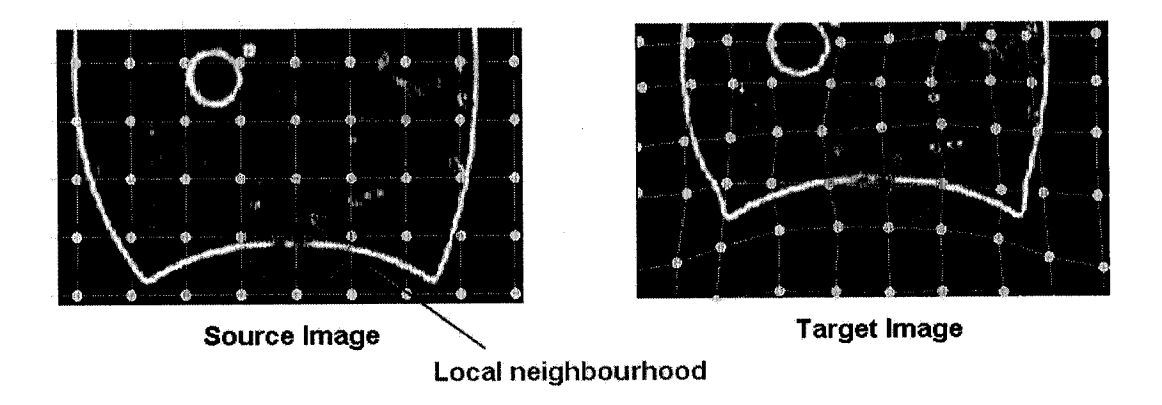


Figure 3–5: Local node deformation strategy. These images show a part of the 3D lattice overlaid on the gradient magnitude data. Under the current transformation, the node \vec{x} is mapped to $\mathbf{N}(\vec{x})$ on the target image. A small displacement \vec{d} (indicated by the arrow) toward the inner edge of the lung boundary is necessary to maximize the neighbourhood correlation for this node. This is found through optimization of the three translational parameters (dx, dy and dz).

The local neighbourhood of \vec{x} is specified by the ensemble of interpolated feature values from each sub-lattice node defined above. Before optimization, the corresponding neighbourhood in the target volume is defined by transforming each sub-lattice node by the current non-linear transformation N and interpolating the feature value on the target volume. The vector \vec{d} is found using a three-dimensional Simplex optimization procedure, maximizing the correlation between the two sub-lattices (Fig. 3–5). At each step of the optimization procedure, the coordinates of the target sub-lattice are modified, the feature values re-interpolated, and the correlation between the two sub-lattices calculated. The optimization procedure stops when the normalized difference between the maximum and minimum correlation values, evaluated at the simplex vertices, is smaller than a preset tolerance.

Smoothing constraints. Since a continuous deformation field is required, the estimation process must be constrained so that it cannot compress two distinct points together or allow an overlap, nor can it induce a tearing of the field. This is achieved by tempering the deformation vector above with the average of the deformation vectors of the neighbouring nodes. If $\mathbf{M}(\vec{x})$ is the mean deformation vector calculated from the immediate neighborhood of \vec{x} , then the resulting deformation is given by:

$$\vec{d}' = \beta \mathbf{M}(\vec{x}) + (1 - \beta)\vec{d}, \quad with \quad 0 \le \beta \le 1.0.$$
 (3.15)

A large value of beta ensures a very smooth deformation field at the expense of possibly missing some small local variations, while a small value of beta gives more importance to the estimated deformation vector, with the risk of permitting local discontinuities to pass into the global deformation field. It was found that β =0.5 yields an acceptable balance between local matching and global smoothness.

Iterative refinement. Since the deformation at a single node is part of a continuous global warp, it affects not only that node, but all neighboring nodes as well. The correlation values for those neighbouring nodes will also change as a result. Consequently, an iterative approach is used, where a fractional value of the estimated deformation is stored for each node at each iteration until the deformation vector reaches convergence when a pre-defined number of iterations is reached. This approach dampens the tendency for artifactually large local shifts to introduce irreversible distortion in the deformation field. A value of 0.6 was found to be a good compromise between robustness and speed of convergence.

CHAPTER 4

Phantom-based Verification Methods for Motion Management

The purpose of this chapter is threefold: (1) to describe the mechanics and magnitude of the respiratory motion in a real lung; (2) to review commercially available lung phantoms and those described in the literature; (3) to summarize the features and applications of an "ideal" deformable lung phantom.

4.1 Ideal lung phantom: the human lung

The mechanics of breathing. Respiration is an "involuntary" action, *i.e.*, a person would continue to breathe despite being unconscious. Unlike cardiac motion, the respiratory motion is not rhythmic. The periodic cycle of respiration is regulated through chemoreceptors by the levels of CO_2 , O_2 and pH in the arterial blood.

Anatomically, the lungs are held within the thoracic cavity, encased by the liquid-filled intrapleural space. Inhalation requires active participation of respiration muscles. During the inhalation part of quiet breathing, the increasing volume of the thoracic cavity draws air into the cavity. The most important muscle of inhalation is the diaphragm. As the diaphragm is contracted, it descends and the abdomen is forced inferiorly and anteriorly, increasing the superior-inferior (SI) dimension of the chest cavity. The intercostal muscles connect adjacent ribs and also participate in normal inhalation. They contract during inhalation, pulling the ribs superiorly and anteriorly, thereby increasing both the left-right (LR) and anterior-posterior (AP) dimensions of the thorax. Exhalation is passive for quiet breathing. The lung

and chest walls are elastic and return passively to their pre-inhalation positions at exhalation. Other ventilation muscles are involved only during active exhalation.

Transpulmonary pressure, the pressure difference between respired gas at the mouth and the pleural pressure around the lungs, is reduced during inhalation and is recovered during exhalation. During normal breathing, the deflating lung volume is larger than the inflating volume at the same transpulmonary pressure. This is called "hysteresis", attributable to the complex respiratory pressure-volume relationship of the lung and chest wall.

During normal respiration, the lung volume typically changes by 20% (from 3.3 l to 4.1 l on average, as determined in a 10-patient study [5]); at deep inhalation, the increase in lung volume is approximately three to four times that of normal breathing [79].

Measurement of respiratory motion. Patients' breathing patterns can vary in magnitude, period and regularity during imaging and treatment sessions [28, 29, 98, 111], as shown in Fig. 4–1. Systematic changes in the respiratory baseline may also occur. Motion also varies markedly between patients, indicating that an individual approach to respiratory management is advised.

Respiratory motion studies have tracked the movement of the tumour [4, 19, 31, 33, 91, 101, 102], the host organ, radiographic fiducial markers embedded at the tumour site [98, 10, 64, 75, 51] and surrogate organs, such as diaphragm, which are assumed to correlate with the tumour [25, 69]. This data is summarized in Table 4–1.

The amount a lung tumor moves during breathing varies widely. Stevens et al. [102] found that out of 22 lung tumor patients, 10 subjects showed no tumor

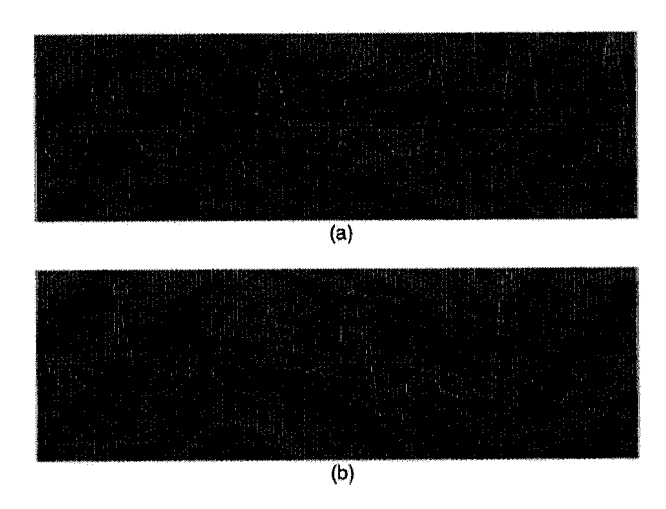


Figure 4–1: Variations in respiratory patterns from the same patient taken a few minutes apart. The three curves in each plot correspond to infra-red reflector measured patient surface motion in the SI, AP, and RL directions, with each component arbitrarily normalized. In (a), the motion pattern is relatively reproducible in shape, displacement magnitude, and pattern. In (b), the trace is so irregular that it is difficult to distinguish any respiratory pattern. Reproduced from [45].

Table 4–1: SI, AP and LR lung tumour-motion data. The mean range of motion and the (minimum-maximum) ranges in milimiters for each cohort of subjects. Reproduced from [45].

		Direction	
Observer	SI	AP	LR
Barnes et al. [4] Lower lobe	18.5 (9-32)	-	-
Middle, upper lobe	7.5(2-11)	-	-
Chen <i>et al.</i> [10]	(0-50)	-	-
Ekberg et al. [18]	3.9(0-12)	2.4 (0-5)	2.4 (0-5)
Engelsman et al. [19]			
Middle/upper lobe	(2-6)	-	-
Lower lobe (2-9)	-	-	-
Erridge et al. [20]	12.5 (6-34)	9.4 (5-22)	7.3 (3-12)
Ross et al. [91] Upper lobe	-	1 (0-5)	1 (0-3)
Middle lob	-	1.2(0.6)	9 (0-16)
Lower lobe	-	1 (0-4)	10.5 (0-13)
Grills et al. [31]	(2-30)	(0-10)	(0-6)
Hanley et al. [33]	12 (1-20)	5 (0-13)	1 (0-1)
Murphy et al. [71]	7 (2-15)	-	-
Plathow et al. [80] Lower lobe	$9.5 \ (4.5 \text{-} 16.4)$	$6.1\ (2.5 \text{-} 9.8)$	$6.0\ (2.9 - 9.8)$
Middle lobe	$7.2 \ (4.3-10.2)$	4.3 (1.9-7.5)	$4.3 \ (1.5 - 7.1)$
Upper lobe	4.3 (2.6-7.1)	$2.8 \ (1.2 - 5.1)$	$3.4\ (1.3-5.3)$
Seppenwoolde et al. [98]	5.8 (0-23)	2.5 (0-8)	1.5 (0-3)
Shimizu et al. [99]	-	6.4 (2-24)	-
Sixel et al. [101]	(0-13)	(0-5)	(0-4)
Stevens et al. [102]	4.5 (0-22)	_	_

motion in the SI direction. Of the remaining 12 subjects, the average SI displacement was anywhere from 3 to 22 mm (mean 84 mm). They found no correlation between the occurrence or magnitude of tumor motion and tumor size, location, or pulmonary function, suggesting that tumor motion should be assessed individually. Seppenwoolde et al. [98] measured 3D trajectories for 20 patients via dual real-time fluoroscopic imaging of a fiducial marker implanted in or near the tumor. They observed hysteresis in the trajectories of half of the patients, amounting to a 1 to 5 mm separation of the trajectories during inhalation and exhalation, with 4 out of 20 patients exceeding a 2 mm separation. This indicates that in cases where high accuracy is required in treatment delivery, a real-time tracking or gating process based on surrogate breathing signals should not only correlate with the tumor's motion along each axis, but should also have knowledge of the respiratory phase, because the phase difference is what leads to the hysteresis effect. In Fig. 4–2, motion trajectories during radiotherapy of lung tumors, measured using implanted gold markers, are depicted.

The review of the respiratory motion literature leads to the following conclusion: There are no general patterns of respiratory behaviour that can be assumed for a particular patient prior to observation and treatment. The many individual characteristics of breathing - quiet versus deep, chest versus abdominal, healthy versus compromised - and many motion variations associated with tumour location and pathology lead to distinct individual patterns in displacement, direction and phase of tumour motion. However, as a general observation, the tumour trajectory length

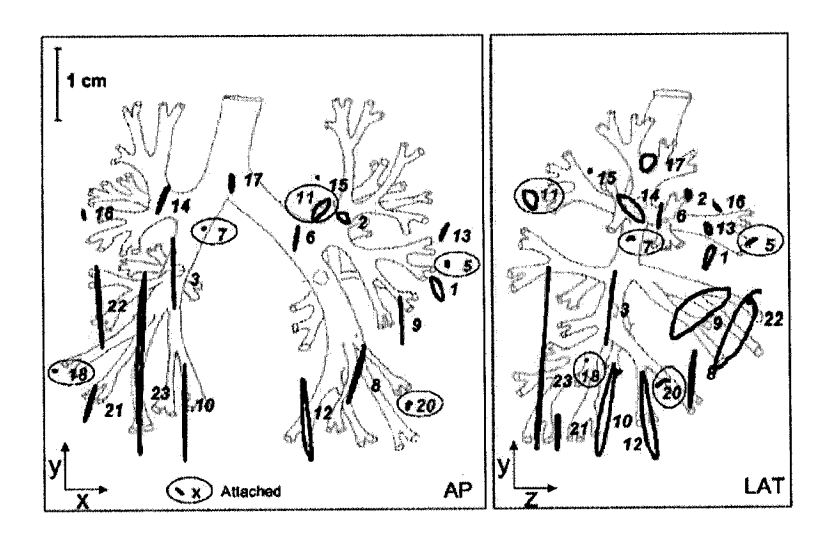


Figure 4–2: Tumour trajectories (not to scale) in 23 lung patients, measured using implanted markers and real-time stereoscopic fluoroscopy. Reproduced from [98].

in the SI direction is higher in the lower and middle lobs of the lung (see Table 4–1 and Figure 4–2)

4.2 Literature review on existing phantoms

The problem of motion in radiotherapy has been approached in the literature with the aid of experiments with numerous incentives .

Rietzel et al. [86] used a set of spherical and triangular objects placed on a one-dimensional moving platform to analyze, validate and improve the performance of the 4D CT protocol. Ford et al. [24] performed validation measurements of a 4D CT dataset using a phantom with an elliptical moving sphere designed to simulate respiratory-induced tumor motion.

Li et al. [57] developed a method to perform 4D CT scans at a relatively low current, in order to reduce the radiation exposure of the patients and tested their

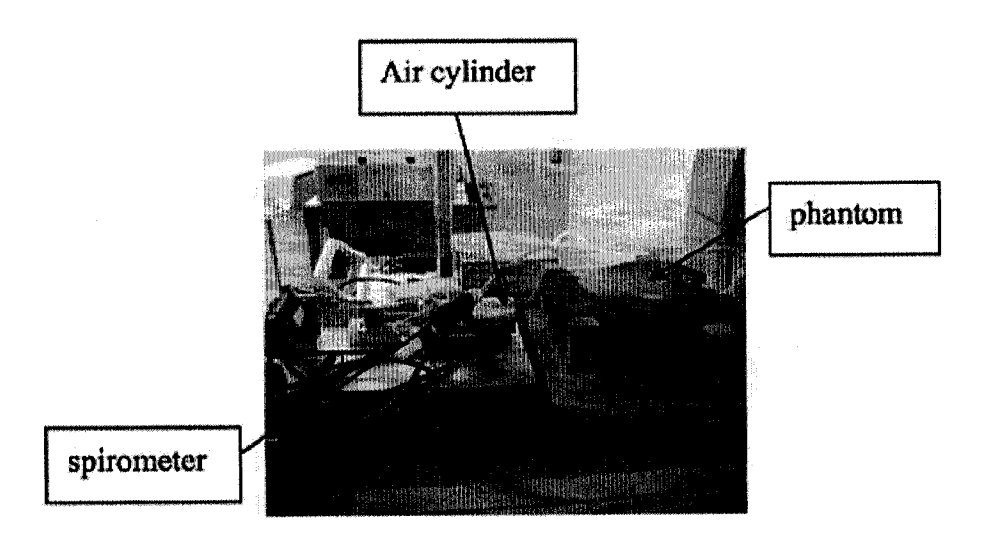


Figure 4–3: Experimental setup of the simulated respiratory phantom. An air cylinder is used to simultaneously drive air in and out of the balloon and the input port of the ABC system. Reproduced from [17].

method using a rigid anthropomorphic thorax phantom placed on a platform capable of sinusoidal motion in the SI direction.

D'Souza et al. [17] used the active-breathing control (ABC) system to implement gated CT acquisition using flow-volume spirometry and tested their prototype by designing two motion phantoms: the first phantom simulated a tumour attached to an inflatable balloon, which changed position as a function of air-flow in the simulated lung (Fig. 4–3). The second phantom consisted of an anthropomorphic rigid phantom (Rando) placed on a 1D sinusoidally moving platform (Fig. 4–4).

Lu et al. [59] tested the accuracy of the deformable registration algorithm by using a gel-balloon deformable phantom. In this phantom, a balloon and 320 plastic beads implanted around the balloon in a regular cube grid were imersed in gel, and could be inflated and deflated with insertion or removal of heavy oil. The

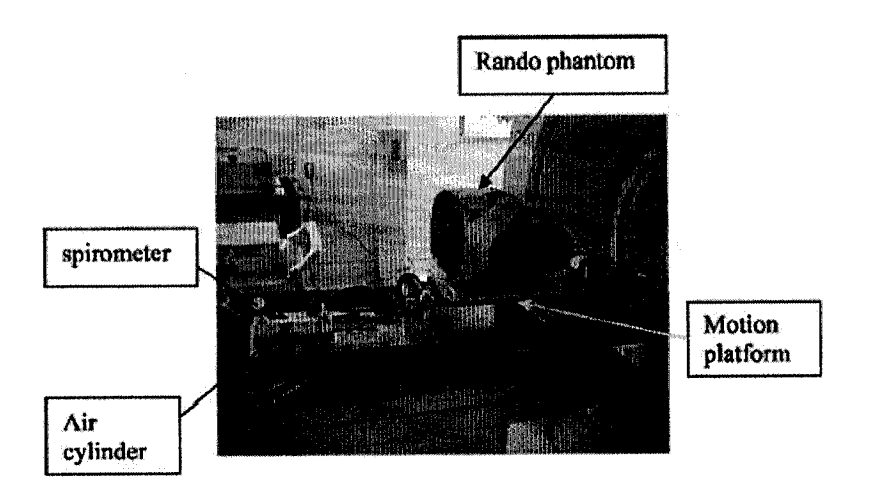


Figure 4–4: Experimental setup of the anthropomorphic phantom (Rando phantom) on the moving platform. The platform drives the phantom in a sinusoidal manner. The platform is connected to a piston that drives air in and out of a cylinder whose output port is connected to the receiving port of the ABC system. Reproduced from [17].

deformable image registration of the phantom corresponding to a displacement of the plastic beads of 3-4 mm between the inflation-deflation stages was reported with an accuracy of less than 1 mm (Fig. 4-5).

A number of authors used rigid motion phantoms to investigate intra-fractional organ motion effects in IMRT treatments. Jiang et al. [38] investigated how the intra-fractional organ motion effects in lung IMRT treatments delivered by multileaf collimator influenced the prescribed dose by using solid water placed on a 1D sinusoidally moving platform. Keall et al. [44] has developed and demonstrated the feasibility of a motion adaptive radiation therapy delivery on a sinusoidally moving target (i.e., a diode detector), for both uniform field and IMRT field treatments. Alasi et al. [1] used a rigid 1D moving phantom to assess the dynamic delivery

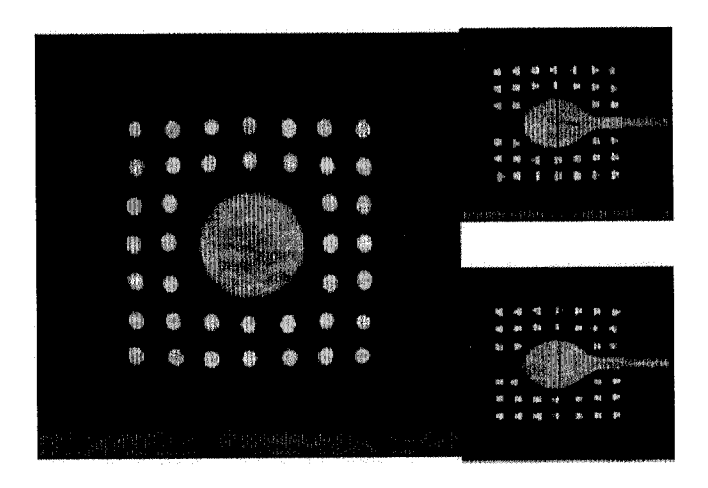


Figure 4–5: The registered version of the gel-balloon deformable phantom designed by Lu *et al.*. The red component is the reference stage and the green component is the registered test stage. Reproduced from [59].

method where the MLC motion is synchronized with the phantom motion. Schaefer et al. [95] used a cylindrical phantom mounted on a 1D moving platform to study the contribution of interplay effects in IMRT to the thorax.

Nioutsikou et al. [74] studied the effects of 3D organ and tumour motion to the degradation of 3D CRT and IMRT planned dose distributions using an anthropomorphic, tissue-equivalent, deformable phantom. The phantom consisted of two accordion-type flexible bottles filled with dampened sponges and an inserted solid tumour, holding Gafchromic EBT film, that could be driven in any arbitrary 3D trajectory (Fig. 4–6). Whereas the phantom allowed the authors to experimentally verify the effect of tumour motion on the dose distribution, their phantom design could not be used for deformable registration necessary in the application of 4D treatment planning.

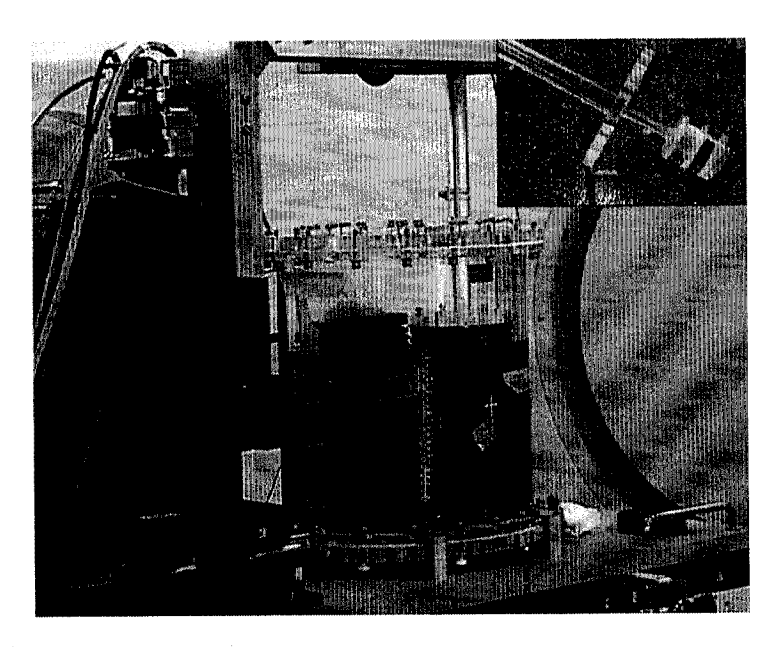


Figure 4–6: Deformable breathing phantom, standing on the treatment couch. The inset shows one of the Perspex tumours, with three film inserts pointed by the arrows, that was placed in the right lung. Reproduced from [74].



Figure 4–7: The diagnostic phantom with the abdominal insert removed (left), and the high density foam insert (right) that extended the existing lung insert. Reproduced from [39].

Kashani et al. [39] developed a deformable lung phantom by removing the abdominal insert from a diagnostic thoracic phantom and extending the existing lung insert with high density foam infused with iodine, in order to mimic lung attenuation properties at diagnostic imaging energies (Fig. 4–7). The foam was compressed and decompressed by an actuator-driven diaphragm. Rigid tumour-simulating inserts were embedded in the foam and their 1D motion characteristics and reproducibility were studied.

One commercially rigid phantom, designed to investigate and minimize the impact of organ motion and patient positioning errors in radiation therapy, is that constructed by CIRS, Model 008 Dynamic Thorax Phantom (Fig. 4–8). Major components of the system include a tissue equivalent thorax phantom, a precision motion actuator and controller with pre-set motion profiles. Three-dimensional motion of the tumors in the phantom are achieved by the actuator applying synchronized linear

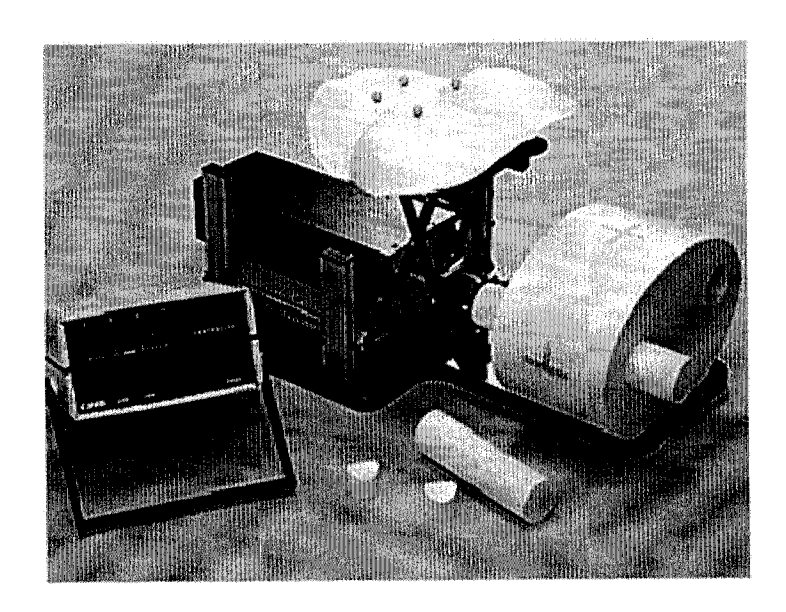


Figure 4-8: CIRS Model 008 Dynamic Thorax Phantom.

and rotational motion to a moving rod. Sinusoidal and other complex motions can be achieved with sub-millimeter accuracy and reproducibility.

4.3 Features and applications of a designed, ideal lung phantom

As presented in Section 4.2, the commercially available lung phantoms and most of those described in the literature are rigid objects or phantoms with an imposed 1D or 2D motion. The existing deformable lung phantoms are limited in their capability of reproducing a real lung 3D non-isotropic lung deformation/motion or the differential motion at different locations in the phantom as described in Section 4.1. Moreover none of the presently constructed deformable phantoms can be used in quality assurance of all aspects of 4D radiotherapy, namely, the 4D computed to-mography, the 4D treatment planning and the 4D treatment delivery.

The properties of an ideal lung phantom would include complex geometry, anisotropic inflation and composition, lobar structure and internal airway architecture similar to that of human lung. Applications of such a phantom would be as follows:

- 1. Evaluation of respiratory motion effects during CT image acquisition as well as validation of 4D CT procedures for irregular breathing patterns.
- 2. Evaluation of the accuracy of the deformable image registration.
- Testing and calibration of various real-time tumor localization and tracking devices.
- 4. Measurement of the delivered dose taking into account the change in lung volume during the breathing cycle and the distortions of the dose distribution due to the deforming lung.
- 5. Evaluation of a 4D-optimized treatment plans that incorporate the effects of breathing motion.
- 6. Validation of 4D dose calculation algorithms in deformable/moving targets.
- 7. Dosimetric and positional verification of individual patient treatment plans before treatment with motion mitigation techniques.

The proposed deformable lung phantom described in *Chapter 5* attempts to complement the existing phantoms by adding new features, that makes it suitable for use in the 4D IGRT validation process.

CHAPTER 5

Design, Construction and Performance of a Novel Deformable Lung Phantom

This chapter presents the design, construction and performance of the deformable lung phantom we developed. The experiments in this chapter are divided into four parts: (1) evaluation of the mean mass density of the simulated lung material and the relative mass density change between the PI and PE breathing states; (2) 3D motion assessment at different locations in the phantom; (3) 3D motion reproducibility; (4) deformable image registration of PI and PE breathing phases of the phantom and validation of the deformable image registration.

5.1 Phantom construction

The prototype design for the deformable phantom is presented in Fig. 5–1. The phantom is operated horizontally with its axis coinciding with the CT z-axis. The lung is simulated as a natural rubber latex balloon filled with slightly dampened natural yellow sponges. The balloon is mounted inside a Lucite cylinder that simulates the thoracic cavity. The space around the lung is filled with water which replicates the chest mass. At the superior end the lung is left open for air communication through a perforated lid (vent holes), which keeps the sponge in place inside the balloon. At the inferior end, the lung is attached to a 10-cm thick Lucite piston, made to fit the cylinder. The piston, simulating the diaphragm, is fastened to a programmable motor via a metal rod, which compresses and decompresses the lung

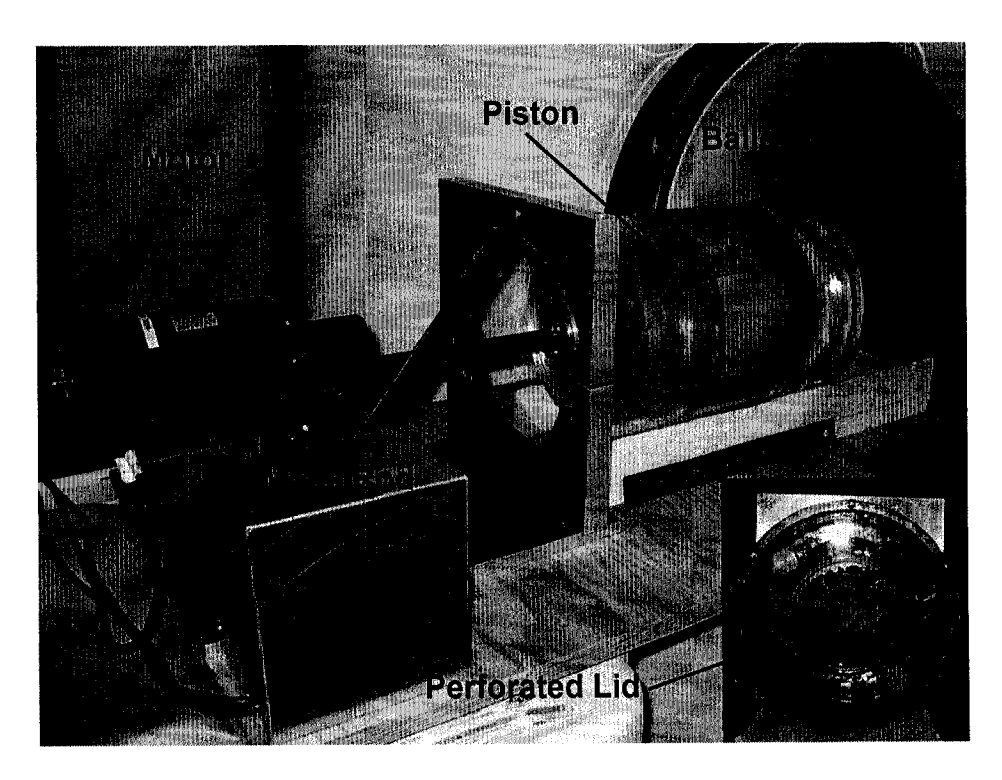


Figure 5–1: Prototype of the deformable phantom. The inset shows the top view of the phantom.

according to an arbitrary, programmable breathing profile. This assembly simulates the respiratory motion of the diaphragm in the superior-inferior direction while lung tissues have a 3D non-isotropic motion/deformation (Fig. 5–2). Various motion profiles can be programmed so that the phantom is capable of simulating measured, irregular breathing patterns with varying periods and amplitudes.

5.2 Simulation of lung tissue

The natural sponges (Fig. 5–3(b)) are slightly dampened in order to simulate the density of lung tissue and hence the desired Hounsfield (CT) numbers in computed tomography. A deformable, elliptical, tissue equivalent tumour made of Dermasol,

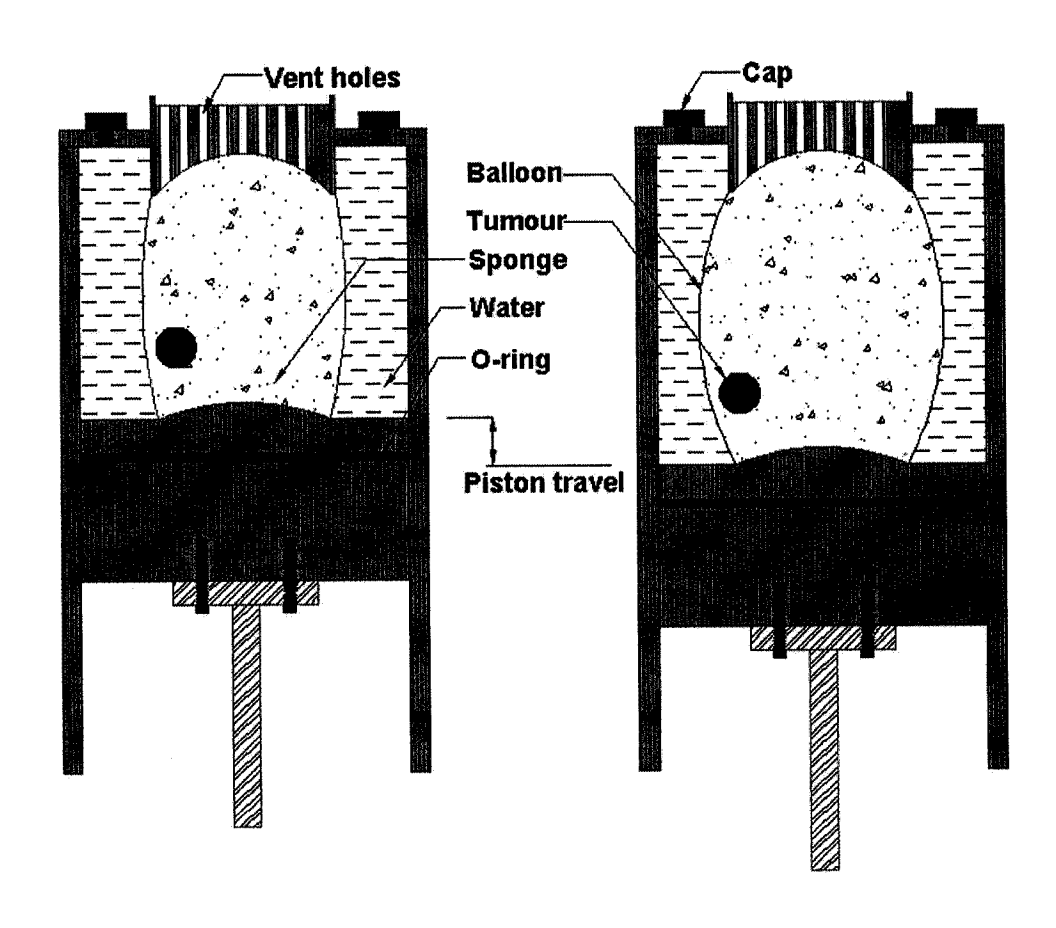


Figure 5-2: Principle of deformable lung inflation as realized with the lung phantom.

density of 0.818 g/cm³, is embedded in the sponge (Fig. 5–3(c)). Dermasol is a new medical device material made from Thermoplastic Elastomer (TPE) (California Medical Innovation, Pomona, California). The tumour has several incisions to hold radiochromic film (Gafchromic, EBT). The film can be positioned before imaging of the phantom and remains in place for the delivery of the treatment plan. In this way, the location of the measuring point or area can be accurately determined for the purpose of comparison with alternative dose measurement methods or with dose calculations.

Nylon wires and Lucite beads (Fig. 5–3(c)), emulating vascular and bronchial bifurcations, were uniformly glued at various locations throughout the natural sponges. The beads and bifurcations act as unique features which assist the deformable registration procedure and also serve as landmarks for quantifying the accuracy of the deformable registration of the phantom images. The tumour, the Nylon wires and Lucite beads can be visualized in a 3D volume rendering of the phantom sectioned along a longitudinal plane in Fig. 5–3(a).

5.3 CT data acquisition

CT data was acquired on both a General Electric (GE) 64-slice LightSpeed VCT scanner and a Philips AcQSim CT scanner, following a helical scanning protocol, at an image resolution of $0.7 \times 0.7 \times 1.25$ mm³ and $0.7 \times 0.7 \times 3$ mm³, respectively. For the 3D motion assessment, eight 3D image datasets of the static phantom (corresponding to PE - Peak Exhale; EI - Early Inhale; MI - Mid Inhale; LI - Late Inhale; PI - Peak Inhale; EE - Early Exhale; ME - Mid Exhale; LE - Late Exhale), at an image resolution of $0.7 \times 0.7 \times 1.25$ mm³, were obtained for eight equally spaced diaphragm

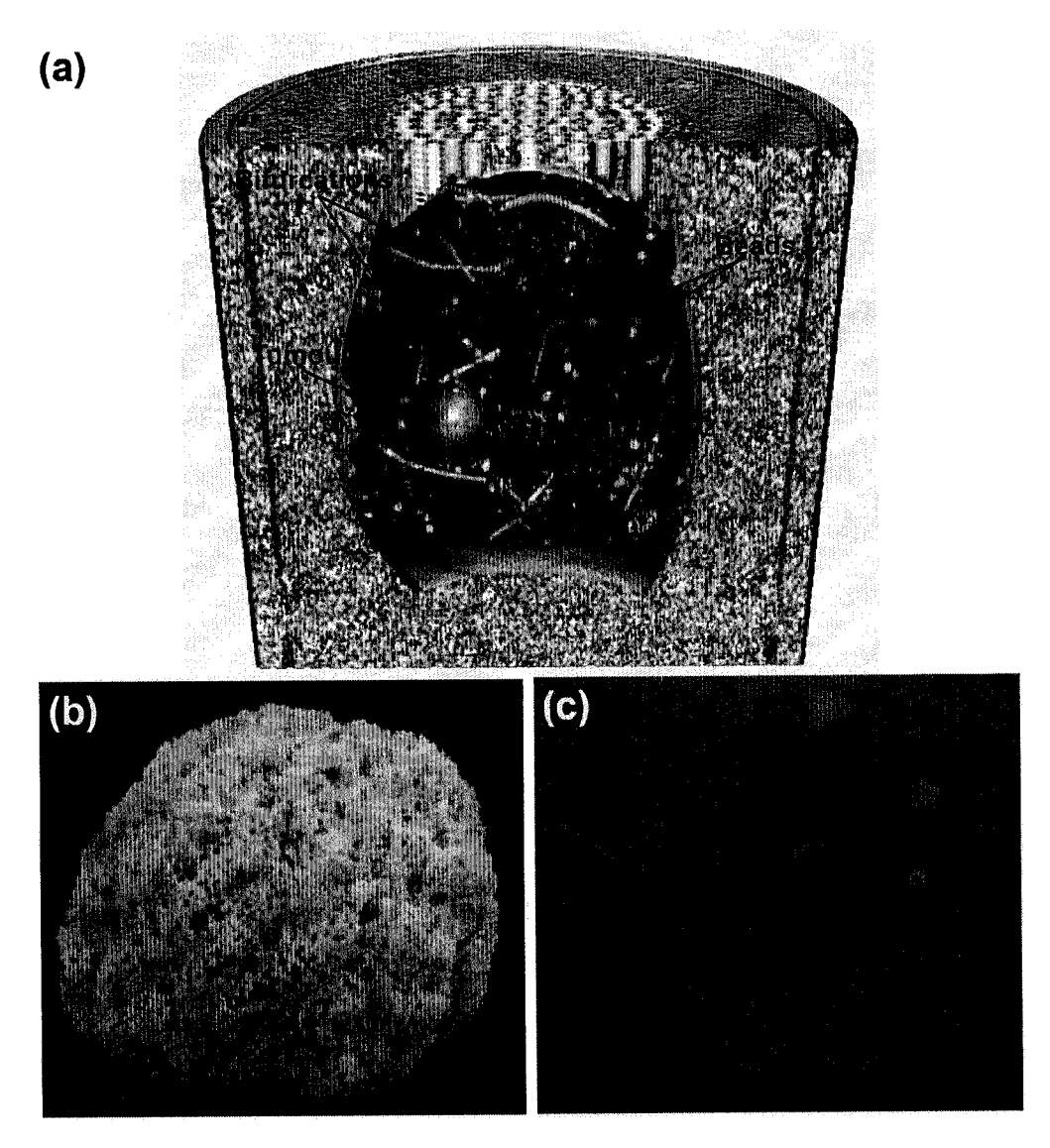


Figure 5–3: (a) Simulation of the vascular and bronchial bifurcation in a 3D volume rendering of the phantom, sectioned along a longitudinal plane; (b) natural sponge; (c) Dermasol tumours of different sizes (1), Nylon wires in form of bifurcations (2), Lucite beads (3).

positions. The amplitude of piston motion was 1 cm, or 2 cm peak-to-peak. To evaluate motion reproducibility of the lung, seven repeat CT scans, at an image resolution of $0.7 \times 0.7 \times 1.25 \text{ mm}^3$, were obtained for a given state of compression. Three different states of compression (corresponding to PE, MI, and PI) were checked. Deformable image registration was performed to register PI to PE breathing phases. For this purpose, the two extreme breathing datasets were acquired at two image resolutions, of $0.7 \times 0.7 \times 1.25 \text{ mm}^3$ and $0.7 \times 0.7 \times 3 \text{ mm}^3$.

5.4 Performance of the deformable lung phantom

Expansion of the simulated lung is achieved by piston retraction which provokes a volume increase (elongation) of the "thoracic cavity". As a result, the layer of water of constant volume surrounding the deformable structure (balloon) becomes thinner. The additional volume created this way in the simulated lung is filled by air entering through the vent holes and results in sponge decompression. This arrangement results in a true, 3D non-isotropic deformation of the balloon, similar to a real lung. The initial tests on the phantom were performed for a 20-mm piston excursion and resulted in deformations of the balloon of 20 mm superior-inferior (SI), 4 mm anterior-posterior (AP) and 5 mm left-right (LR). Fig. 5–4 shows a comparison between the CT number histograms in a real lung and the lung phantom. The resulting average and spread in CT numbers for the phantom lung are comparable to those for a real lung.

Table 5–1 shows mean lung mass densities at PE and PI as well as mean lung density changes, lung volume changes and diaphragm displacements between PE and PI for four lung patients and the lung phantom, based on CT number analysis over

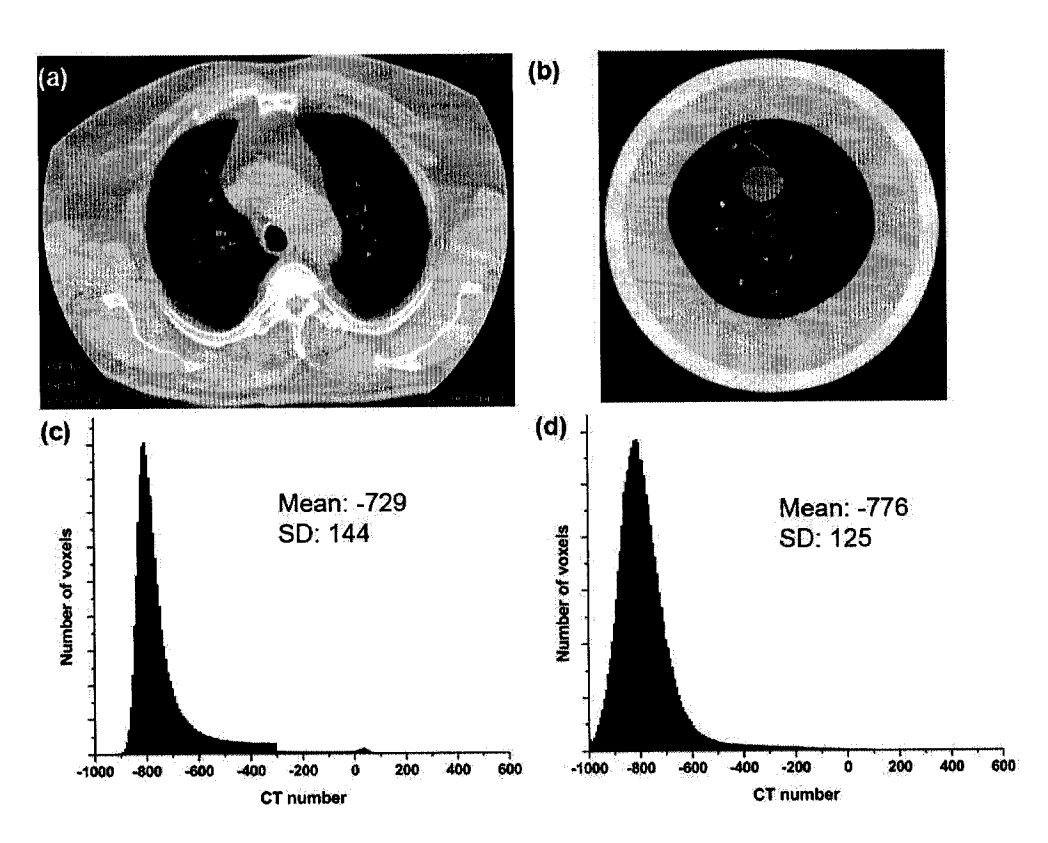


Figure 5–4: Axial CT images of: (a) real lung (free breathing) and (b) phantom lung (early inhale). CT number histograms within the whole lung region for: (c) real lung and (d) phantom lung.

Table 5–1: Mean lung mass densities at PE and PI, lung density changes, lung volume changes and diaphragm displacements between PE and PI for four lung patients and the lung phantom (one SD is given in brackets).

	Density PE	Density PI	Density change	Volume change	Diaphr. Displ.
		•	(PE - PI)/PI	(PI - PE)/PE	PI - PE
	(g/cm^3)	(g/cm^3)	(%)	(%)	(mm)
Patient 1	0.23 (0.19)	0.21 (0.18)	6.47	7.48	11
Patient 2	0.23(0.14)	0.21(0.13)	8.77	10.65	13
Patient 3	0.29(0.16)	0.25(0.16)	11.53	21.40	23
Patient 4	0.33(0.20)	0.28 (0.16)	18.18	28.19	25
Phantom	$0.24 \ (0.12)$	0.19 (0.19)	18.18	40.00	20

the full lung volume. From Table 5–1 it can be noticed that there is a large variability in lung mass densities from patient to patient and the mean lung density of the phantom is comparable to density changes observed in patient 4D CT data. Changes in the phantom lung density can be achieved by controlling the level of dampening of the sponges inside the balloon. Table 5–1 also shows that for a 20-mm displacement of the diaphragm, the phantom's lung volume increases by 40%, which is superior to real lung expansion. This could be overcome by using a Plexiglas cylinder of a smaller diameter, which will decrease the lateral expansion of the balloon, and hence reduce the volume change of the balloon for the same diaphragm displacement.

5.5 Assessment of 3D motion and motion reproducibility

To perform a quantitative 3D motion analysis at different points in the phantom, the locations of 12 anatomical point landmarks uniformly spread within the lung volume were manually identified on the eight CT datasets acquired throughout the respiratory cycle. The position of each landmark was plotted as a function of the respiratory phase in order to generate 3D landmark trajectories. Image intensity

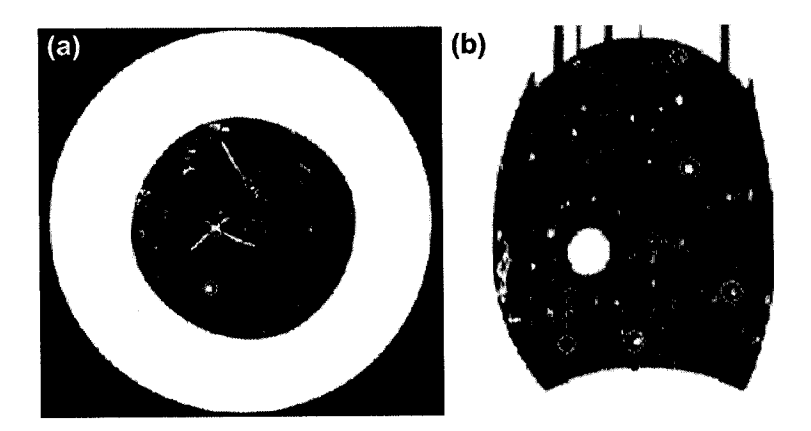


Figure 5-5: Example of manually chosen point landmarks.

thresholds were used to automatically outline the tumour on the eight respiratory phases and the center of mass (COM) of the tumour, determined on each image set, was used to quantify tumour motion. To evaluate the reproducibility of the phantom motion seven point landmarks were identified in each CT dataset. The positions of the corresponding landmarks through the seven repeats of the same breathing phase were compared. Examples of manually selected landmarks are shown in Fig. 5–5.

The tumour COM LR, AP, and SI trajectories inside the lung phantom, during a complete simulated breathing cycle, are shown in Fig. 5–6(a). Fig. 5–6(b) shows the SI trajectories of the twelve selected landmarks and tumour's COM during a complete breathing cycle, highlighting differential motion at different locations in the phantom. The maximum SI motion magnitude at different landmark positions (Table 5–2) for a given excursion of the piston is related to the initial distance of the landmark to the piston and varies between 94% and 3% of the 20-mm diaphragm excursion for positions closer and farther away from the diaphragm, respectively.

As expected, landmarks closer to the diaphragm moved farther than those more superiorly positioned (Fig. 5–6(c)), similar to the situation in a real lung. Radially, the larger the distance of the selected landmark from the central axis of the phantom, the larger is their radial displacement upon deformation. As can be seen from Fig. 5–6(d) this trend holds for all landmarks except from landmarks no. 1, 2, 4 and 9. Landmarks no. 1 and 2 are located in the superior part of the phantom where the radial motion is constrained by the Lucite sleeve holding the upper portion of the balloon. Landmarks no. 4 and 9 are on the posterior part of the lung where the displacement of the landmarks is less than on the anterior part due to Archimedes force exerted on the balloon. Repeat imaging of the phantom at different piston positions, corresponding to different breathing phases, demonstrated excellent motion reproducibility of the selected features inside the phantom, within the image resolution (0.7x0.7x1.25 mm³), which was the limiting factor in accurate identification of the point landmarks.

5.6 Deformable image registration

Deformable image registration was performed using the Automated Nonlinear Image Matching and Anatomical Labeling (ANIMAL) non-linear registration algorithm developed by Collins et al. [13] and applied to the registration of lung anatomies by Heath et al. [34]. The ANIMAL code determines the 3D nonlinear deformation field required to register the two volumes by sequentially stepping through the source volume on a 3D cubic lattice, and estimating at each node the displacement vector required to maximize the correlation coefficient of image intensities in the neighborhood of the node. The algorithm was applied iteratively in a multi-scale

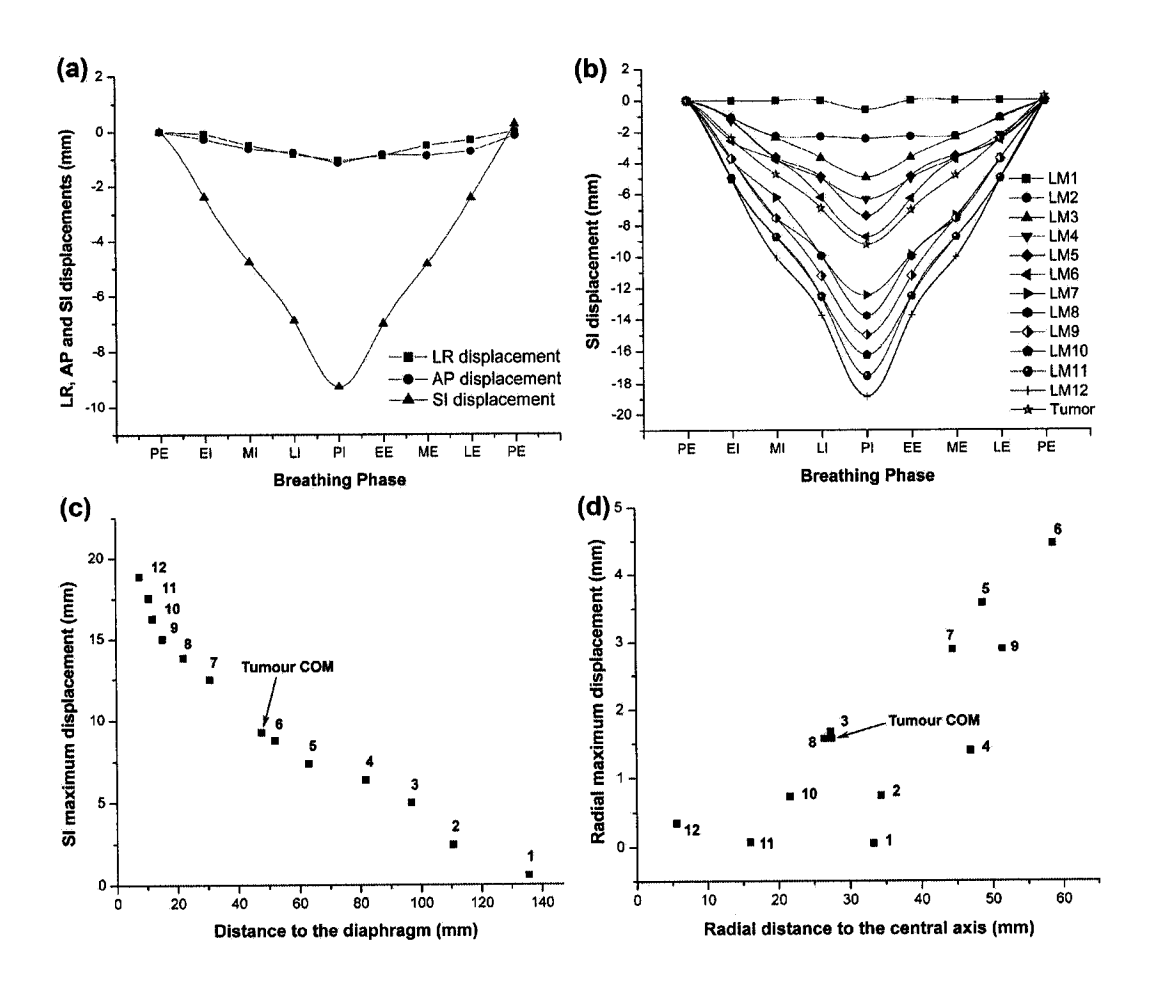


Figure 5–6: (a) Tumour COM LR, AP, and SI trajectories during a complete breathing cycle; (b) SI trajectories for the 12 point landmarks (LMs) and tumour COM during a complete breathing cycle; (c) SI maximum displacements of the landmarks as a function of their initial distance to the piston for a 20-mm excursion of the piston; (d) radial maximum displacement of the landmarks as a function of their initial radial distance to the central axis of the balloon for a 20-mm excursion of the piston.

Table 5–2: Landmark (LM) maximum SI displacements for a 20 mm excursion of the diaphragm, given in millimeters and as percentage of the diaphragm excursion.

LM	Distance to diaphragm	Maximun	n LM displacement
no.	(mm)	(mm)	%
1	135.6	0.6	3.0
2	110.6	2.4	12.1
3	96.9	5.0	24.8
4	81.8	6.4	31.8
5	63.1	7.4	36.8
6	52.1	8.8	43.8
Tumour COM	47.6	9.3	46.3
7	30.8	12.5	62.4
8	22.1	13.8	69.0
9	15.3	15.0	75.1
10	12.1	16.3	81.4
11	10.8	17.5	87.7
12	7.7	18.9	94.3

hierarchy on data at different resolutions, beginning with very blurred data so that gross image features drive the fit at first. The resulting deformation field was then used as a starting point for the next scale step, where less blurred data allow smaller details to be included in processing, thus refining the fit.

The PE and PI images were chosen as the target and source volumes, respectively. An initial linear registration of these two volumes was performed. The recovered linear transformation was applied to the source image and the image intensities were re-sampled on the original voxel grid by tri-linear interpolation. This transformed source image and the initial target image were consequently used as input images for the non-linear registration. The non-linear registration was performed only on the portions of the images containing the balloon and diaphragm. Voxels outside these masked regions have no influence on the image similarity evaluation

during the non-linear registration and were not considered by the registration algorithm when evaluating the image similarity.

The first iteration of the outer loop employed input images blurred using an isotropic Gaussian kernel with FWHM equal to 16 times the image resolution. At this current scale step the deformation field lattice spacing must be no greater then FWHM/2 (8 times the image resolution) to recover the function without aliasing, according to the Nyquist sampling limit. Image blurring and lattice grid spacing were reduced after each iteration, with each successive step refining the estimation of the previous step.

At each scale step of the outer loop, the inner loop recovers the deformation vector at each node in an iterative manner by minimizing an objective function which maximizes the correlation coefficient in a local neighbourhood of that node whilst penalizing deformation on the order of the deformation lattice spacing. To ensure a continuous deformation field, a fraction of the deformation recovered on each iteration is added to the sum of previous estimates. After each iteration, a global smoothing is performed whereby the deformation at each node is replaced by a weighted sum of the current estimate with the mean displacement of the neighbouring nodes.

Each of these processes was controlled by a number of user-specified registration parameters whose values needed to be optimized on each scale step. The combination of parameters which resulted in a stable, lowest minimum of the global objective function were used for registration.

5.7 Accuracy of deformable image registration

Quantitative assessment of deformable registration algorithm accuracy in medical imaging is challenging because it is very difficult to quantify and track temporal anatomy variations in patients or phantoms. The validation of deformable registration may be based on a comparison with a known deformation field [112]; the distance to agreement (DTA) of landmarks [34, 65, 85]; consistency testing [37, 116, 117]; image similarity metrics [34]; 2D/3D contour distance to agreement [34]; and visual inspection (image, contours) [65].

Image registration performance can be limited by residual image artifacts in 4D CT datasets, as well as by spatial resolution. In this work a true retrospectively sorted 4D CT dataset of the breathing phantom was replaced by an artifact-free 4D dataset where each image dataset was obtained for a different compression state of the static phantom. The registration was performed between the extreme breathing phases corresponding to the largest deformations and hence where the largest registration error is expected.

In this study, we evaluated the accuracy of the deformable image registration using both quantitative and qualitative metrics.

Two metrics were used to assess the accuracy of deformable registration after each resolution step: the distance-to-agreement (DTA) of both manually identified point landmarks and triangulated surfaces obtained from 3D structure surfaces.

The DTA of manually identified point landmarks includes a comparison of the predicted and actual displacement of the landmarks on the two images. For this purpose, 37 homologous point landmarks, uniformly distributed within the lung,

were manually identified on the source (PI) and target (PE) images, independent of the registration process. The predicted target landmarks positions were determined by transforming the source landmarks positions using the recovered deformation field by interpolation at the source landmark's location. The accuracy of how well the registration process brings these landmarks into alignment was evaluated by the mean value and the standard deviation of the differences between the actual and predicted target positions along SI, AP and RL directions and also summed in quadrature as a 3D error vector.

The registration accuracy based on the comparison of the predicted and actual displacement of landmarks on the two image datasets is given in Table 5–3. A limiting factor in the registration accuracy evaluation is the accuracy with which homologous landmarks can be identified. Therefore landmark selection was repeated by three independent observers. Mean landmark positions of those landmarks reproducibly identified within 1 slice (1.25 mm) and 2 pixels (1.4 mm), were further used for registration accuracy evaluation. The final vector average registration accuracy, evaluated on the deformation vectors recovered on the 2.1 mm deformation lattice spacing, was 0.55 (0.41 SD) mm, with 0.32 (0.29 SD) mm AP accuracy, 0.27 (0.30 SD) mm LR accuracy and 0.36 (0.25 SD) mm SI accuracy. Further refinement of the registration by going to smaller lattice spacing would only result in a small accuracy improvement at the expense of drastically more CPU time. The computation time for the 2.1 mm lattice spacing was about 1.15 h on a PC Pentium 4 (2.5 GHz, 4 GiB RAM). It can be noticed that the 2.1 mm lattice spacing brings the registration accuracy to the image resolution level.

Table 5–3: Accuracy of the deformable image registration of PI and PE CT datasets for an image resolution of 0.7x0.7x1.25 mm³ (one SD is given in brackets).

Lattice spacing	AP	LR	SI	3D Vector
(mm)	(mm)	(mm)	(mm)	(mm)
$5.6 \times 5.6 \times 5.6$	1.12 (1.20)	0.88 (0.77)	1.14 (1.34)	1.82 (1.96)
$2.8 \times 2.8 \times 2.8$	0.45(0.40)	0.42(0.40)	0.59(0.89)	0.85(1.06)
$2.1 \times 2.1 \times 2.1$	0.32(0.29)	0.27(0.30)	$0.36 \ (0.25)$	$0.55 \ (0.41)$

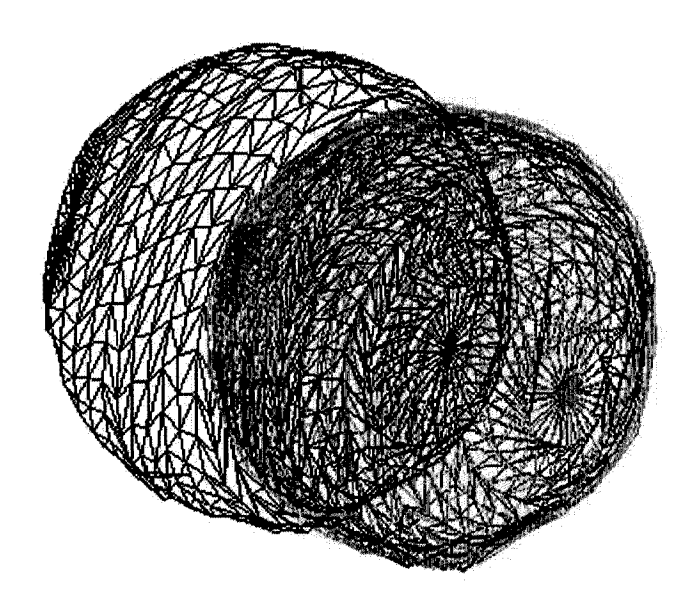


Figure 5–7: Overlap of 3D triangulated surfaces of the tumour at PI (black), PE (orange) and deformed PI (green).

For the DTA analysis of triangulated surfaces, the tumour and lung were automatically contoured using image intensity thresholds on an Eclipse Treatment Planning Station (Varian Medical Systems, Palo Alto). 3D triangulated surfaces were subsequently created from these contours by connecting contour points on adjacent CT slices according to the procedure developed by Heath et al. [34], also illustrated in Fig. 5–7. The triangulated surfaces of the contoured objects in source image are deformed using the recovered deformations for both the tumour and lung. The centre of mass (COM) of the triangulated surfaces of the outlined volumes in the deformed source and target images were determined after each registration step. A 3D mean DTA was calculated by averaging the minimum distances between the deformed source surface and the target surface, evaluated along the normal to each triangle of the deformed surface. The distribution of the 3D mean DTA could be visualized by assigning a colour map to the triangles of the deformed surface based on the closest distance for each triangle [34].

The registration accuracy based on tumour and lung 3D mean DTA and COM shifts between the deformed source and target images, are given in Table 5–4. The tumour and lung mean 3D DTA, evaluated on the finest, 2.1 mm, lattice spacing were 0.44 (0.07 SD) mm and 0.99 (0.81 SD) mm, respectively. The corresponding colour maps of the 3D mean DTA for tumour and lung are shown in Fig. 5–8. The tumour and lung residual COM shift after registration were 0.83 mm and 1.55 mm, respectively.

In order to study the effect of spatial image resolution on registration accuracy an additional deformable image registration and accuracy evaluation was performed

Table 5–4: Tumour and lung 3D mean DTA and COM shifts between the deformed source image and target image (one SD is given in brackets).

Lattice	Tumour		I	ung
spacing	COM shift	3D avg. DTA	COM shift	3D avg. DTA
(mm)	(mm)	(mm)	(mm)	(mm)
Pre-registration	10.05	6.33 (3.70)	11.83	10.40 (10.84)
$5.6 \times 5.6 \times 5.6$	1.10	0.59(0.01)	1.76	1.81 (0.78)
$2.8 \times 2.8 \times 2.8$	0.92	0.47(0.41)	1.61	1.35 (0.56)
$2.1 \times 2.1 \times 2.1$	0.83	$0.44 \ (0.07)$	1.55	0.99 (0.81)

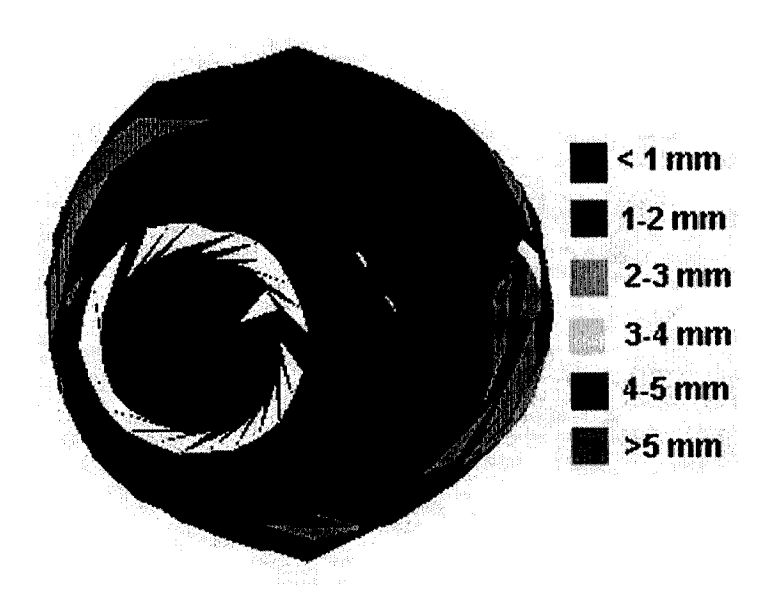


Figure 5–8: Tumour colour-coded representation of DTA. Pink regions of the colour map indicate distance-to-agreement between surfaces greater than 5 mm.

Table 5–5: Accuracy of the deformable image registration of PI and PE CT datasets for an image resolution of 0.7x0.7x3 mm³ (one SD is given in brackets).

Lattice spacing	AP	LR	SI	3D Vector
(mm)	(mm)	(mm)	(mm)	(mm)
5.6 x 5.6 x 5.6	1.04 (1.44)	1.17 (1.52)	1.88 (2.76)	2.44 (3.46)
$2.8 \times 2.8 \times 2.8$	0.42(0.96)	0.64(1.33)	1.13(1.52)	1.36(2.23)
$2.1 \times 2.1 \times 2.1$	0.33(0.62)	$0.66 \ (1.58)$	$1.07 \ (1.65)$	1.30(2.37)

on images acquired at the same extreme breathing phases on a Philips AcQSim CT simulator with an image resolution of $0.7 \times 0.7 \times 3 \text{mm}^3$. This resolution is the usual acquisition resolution for 4D treatment planning and 4D dose calculations. The obtained image registration accuracy is important due to its influence on the 4D dose calculation accuracy. Again, landmark selection was repeated by three independent observers. Mean landmark positions of those landmarks reproducibly identified within 1 slice (3 mm) and 2 pixels (1.4 mm), were further used for registration accuracy evaluation. The registration accuracy based on the comparison of the predicted and actual displacement of landmarks on the two images is given in Table 5–5. Final vector average registration accuracy evaluated on deformation vectors recovered at the 2.1 mm deformation lattice spacing was 1.30 (2.37 SD) mm, with 0.33 (0.62 SD) mm AP accuracy, 0.66 (1.58 SD) mm LR accuracy and 1.07 (1.65 SD) mm SI accuracy.

Since DTA quantification is limited to the neighborhood of the selected landmarks, a qualitative, overall assessment of deformable registration accuracy was performed by visual examination of image overlays. Visual inspection of the overlaid inhale registered to exhale and exhale images showed a good performance of the AN-IMAL registration algorithm (Fig. 5–9). Using red/green image fusion, deviations

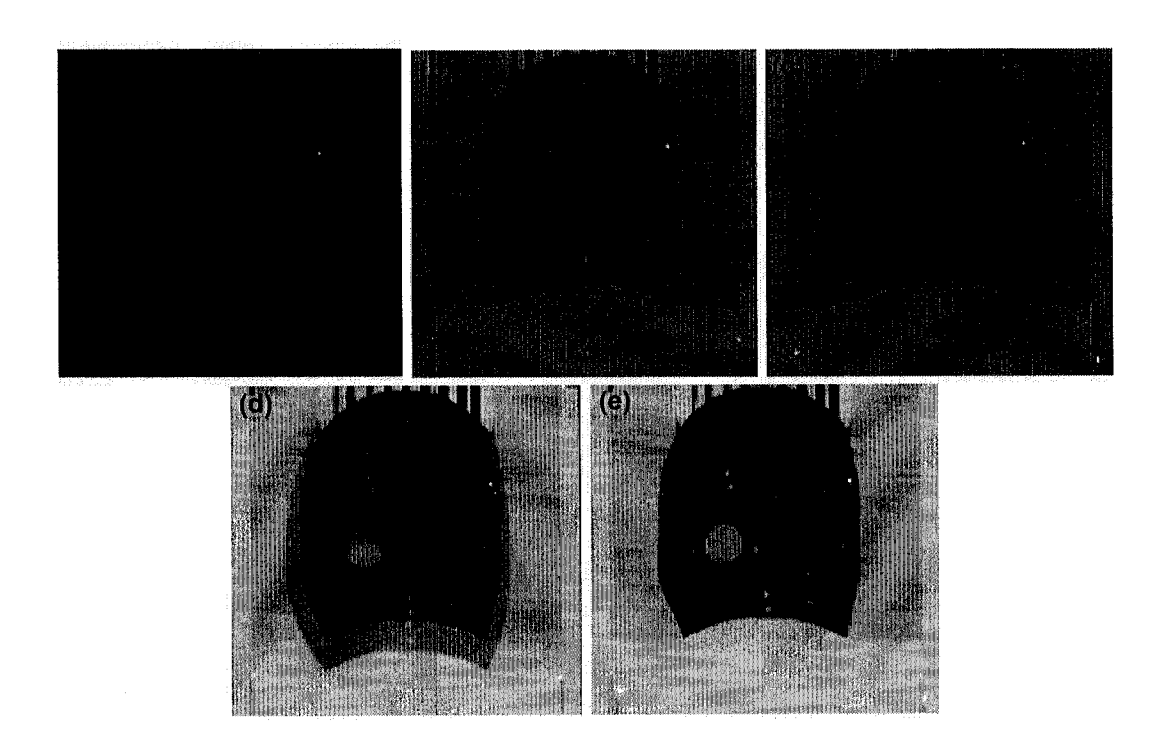


Figure 5–9: Deformable registration of the phantom shown on a coronal cut: (a) Peak Inhale (PI); (b) Peak Exhale (PE); (c) PI deformed to PE (d) PI and PE shown together before registration; (e) PE and deformed PI shown together after registration.

can be clearly identified by red and green areas while matched regions appear in yellow.

CHAPTER 6 Conclusions

An aspiration of radiotherapy has always been to improve geometric as well as dosimetric accuracy. Yet the newest challenge in modern, high-precision IMRT is to deliver the prescribed intensity profile to a moving target. Intra-fractional organ motion is mostly an issue for organs situated in the chest and abdomen, with the lung being of most concern due to respiratory motion. Indeed, in the case of early-stage lung disease, radiotherapy aims to improve outcome beyond the currently preferred option of tumour resection. In conventional practice the margin of the treatment beam is extended to cover most of the range of motion of the tumour, leading to a greater volume of normal tissue being treated unnecessarily. Consequently, the motion problem has been studied extensively in recent years and solutions have been suggested, subject to the assumptions made in each approach. Validation of techniques aimed at measuring and minimizing the effects of respiratory motion require a realistic deformable phantom for use as a gold standard since patient studies for the purpose of dynamic imaging and targeting technique verification is not always suitable, due to the fact that ground truth in patient studies is not known. Therefore, a reproducible, tissue-equivalent deformable phantom is critical to proper commissioning and use of new systems for physiological motion management in radiation therapy.

In this work we present the design, construction, performance and deformable image registration of a novel breathing, tissue equivalent phantom with a deformable lung that can reproducibly emulate 3D non-isotropic lung deformations according to any real lung-like breathing pattern.

6.1 Summary of the work performed

The deformable lung phantom proposed in this study brings new features and a larger potential range of applications compared to other commercially available phantoms or to those described in the literature.

The phantom consists of a Lucite cylinder filled with water containing a latex balloon stuffed with dampened natural sponges. The balloon is attached to a piston that mimics the human diaphragm. Nylon wires and Lucite beads, emulating vascular and bronchial bifurcations, were glued at various locations, uniformly throughout the sponges. The phantom is capable of simulating programmed irregular breathing patterns with varying periods and amplitudes.

The main feature of this deformable, tissue-equivalent phantom is that it is capable of simulating 3D, reproducible, non-isotropic deformations and differential motion at different locations similar to the situation in a real lung. The maximum SI motion magnitude at different landmark positions for a given excursion of the piston is related to the initial distance of the landmark to the piston and varies between 94% and 3% of the 20-mm diaphragm excursion for positions closer and farther away from the diaphragm, respectively. As expected, landmarks closer to the diaphragm moved farther than those more superiorly positioned. The mean density for the lung phantom varies from 0.19 (0.12 SD) g/cm³ to 0.24 (0.12 SD) g/cm³ for a diaphragm

excursion of 20 mm, which is comparable to density changes observed in patient 4D CT data. The reproducible lung deformation is achieved by piston-provoked volume displacement of water surrounding the deforming balloon. Motion reproducibility was found to be within the image resolution (0.7x0.7x1.25 mm³).

A second new feature of this deformable lung phantom is that the tumour itself is deformable and has a complex but reproducible 3D trajectory induced by the motion/deformation of the surrounding sponge.

A third important and new feature of the phantom is the emulation of the vascular and bronchial bifurcations in the real lung, by using Lucite beads and Nylon wires. These unique features assist deformable image registration and also serve as landmarks for verification of the accuracy of the registration. DIR was performed between the extreme breathing phases and the accuracy of the DIR was evaluated. The final vector average registration accuracy using point landmarks as evaluation metric was found to be 0.55 (0.41 SD) mm on images acquired at a resolution of $0.7 \times 0.7 \times 1.25$ mm³. The tumour and lung COM shift post-registration was 0.83 mm and 1.55 mm, respectively. The 3D mean DTA, post-registration was 0.44 (0.07 SD) mm and 0.99 (0.81 SD) mm, respectively.

A comparison between the registration accuracy for the 0.7x0.7x1.25 mm³ and 0.7x0.7x3 mm³ image resolutions showed that the vector average accuracy error decreases from 0.55 (0.41 SD) mm to 1.30 (2.37 SD) mm for registrations performed at the same deformation lattice spacing. This is due to a decrease in the accuracy with which homologous landmarks could be identified (limited by image resolution) and more blurring in the CT data caused by a larger slice thickness.

6.2 Future work

The studies carried out so far used a synthesized, artifact-free 4D CT dataset, where each image dataset was obtained for a different compression state of the static phantom. Future work will include programming of various motion profiles of the phantom so that it can simulate irregular breathing patterns with different amplitudes and periods. Therefore a true retrospectively sorted 4D CT dataset for irregular breathing patterns can be acquired and the validation of the 4D CT procedure can be performed. Also, simulation of hysteresis trajectories that have been found for some human lung tumours could be envisaged by regulating the flow of air in and out of the perforated lid using valves or by simply blocking and unblocking a number of holes in the lid in a dynamic fashion.

Thus far, the most accurate estimate of the dose in a deforming anatomy was determined by the use of a 4D Monte Carlo dose calculation algorithm [35], which has not yet been directly validated by comparison with measurements. The deformable lung phantom allows radiation dose measurements using radiochromic films in several planes within the tumour and 4D radiation dose calculations in a moving/deformable tumor. Therefore, the phantom will provide a means of a quantitative verification and comparison between a conventional treatment plan, a 4D cumulative dose treatment plan and the actual measured radiation dose received by the target.

To summarize, the proposed deformable lung phantom can be used for the evaluation of respiratory motion effects during CT image acquisition and validation of 4D CT procedures. The phantom lung texture contains unique features facilitating DIR of different CT datasets acquired at various breathing phases. The transformations provided by the DIR allow calculation of the cumulative 4D dose received by the tumour during the breathing cycle so that 4D-optimized treatment plans incorporating the effects of breathing motion can be designed. Moreover, validation of any 4D dose calculation algorithm in a moving/deformable target is possible by a direct comparison to the actual dose delivered to a detector (e.g., radiochromic film) inserted into a deformable tumour. Therefore, the lung phantom we propose is suitable for quality assurance of 4D IGRT.

By injecting a radioactive substance in the tumor, the phantom can be used for the evaluation of respiratory motion effects during Positron Emission Tomography (PET) image acquisitions and validation of 4D PET procedures for irregular breathing patterns.

We envisage that the phantom can also be miniaturized to form an insert in a larger anthropomorphic phantom used for the QA in radiotherapy. This opens up a large number of possible commercial applications.

REFERENCES

- [1] H. Alasti, Y. B. Cho, A. D. Vandermeer, A. Abbas, B. Norrlinger, S. Shubbar, and A. Bezjak. A novel four-dimensional radiotherapy method for lung cancer: imaging, treatment planning and delivery. *Phys. Med. Biol.*, 51:3251–3267, 2006.
- [2] M. Austin-Seymour, I. Kalet, J. McDonald, S. Kromhout-Schiro, J. Jacky, S. Hummel, and J. Unger. Three dimensional planning target volumes: a model and a software tool. *Int. J. Radiat. Oncol. Biol. Phys*, 33:1073–1080, 1995.
- [3] R. Bajcsy and S. Kovacic. Multiresolution elastic matching. Comp Vision Graphics Image Processing, 46:1–21, 1989.
- [4] E. A. Barnes, B. R. Murray, D. M. Robinson, L. J. Underwood, J. Hanson, and W. H. Roa. Dosimetric evaluation of lung tumor immobilization using breath hold at deep inspiration. *Int. J. Radiat. Oncol.*, *Biol.*, *Phys.*, 50:1091–1098, 2001.
- [5] C. D. Biancia, E. Yorke, C. S. Chui, P. Giraud, K. Rosenzweig, H. Amols, C. Ling, and G. S. Mageras. Comparison of end normal inspiration and expiration for gated intensity modulated radiation therapy (IMRT) of lung cancer. *Radiother. Oncol.*, 75:149–156, 2005.
- [6] J. M. Blackall, A. P. King, G. P. Penney, A. Adam, and D. J. Hawkes. A statistical model of respiratory motion and deformation of the liver. *Lecture Notes in Computer Science*, 2208:1338–40, 2001.
- [7] H. Blomgren, I. Lax, I. Naslund, and R. Svanstrom. Stereotactic high dose fraction radiation therapy of extracranial tumors using an accelerator. Clinical experience of the first thirty-one patients. *Acta Oncol.*, 34:861–870, 1995.
- [8] F. L. Bookstein. Principal warps thin-plate splines and the decomposition of deformations. *IEEE Trans Pattern Anal*, 11:567–85, 1989.

- [9] T. Bortfeld, K. Jokivarsi, M. Goitein, J. Kung, and S. B. Jiang. Effects of intrafraction motion on IMRT dose delivery: statistical analysis and simulation. *Phys. Med. Biol.*, 47:2203–2220, 2002.
- [10] Q. S. Chen, M. S. Weinhous, F. C. Deibel, J. P. Ciezki, and R. M. Macklis. Fluoroscopic study of tumor motion due to breathing: Facilitating precise radiation therapy for lung cancer patients. *Med. Phys.*, 28:1850–1856, 2001.
- [11] G. E. Christensen and H. J. Johnson. Invertibility and transitivity analysis for nonrigid image registration. *J Electron Imaging*, 12:106–17, 2003.
- [12] G. E. Christensen, R. D. Rabbitt, and M. I. Miller. Deformable templates using large deformation kinematics. *IEEE Trans Image Processing*, 5:1435–47, 1996.
- [13] D. L. Collins and A. C. Evans. Animal: validation and applications of nonlinear registration-based segmentation. Int J Pattern Recogn Artificial Intelligence, 11:1271–94, 1997.
- [14] Intensity-Modulated Radiation Therapy Collaborative Working Group (IMRT CWG). Intensity-modulated radiotherapy: Current status and issues of interest. Int. J. Radiat. Oncol. Biol. Phys, 51:880-914, 2001.
- [15] J. R. DeQuardo, M. S. Keshavan, F. L. Bookstein, W. W. Bagwell, W. D. K. Green, and J. A. Sweeney. Landmark-based morphometric analysis of first-episode schizophrenia. *Proceedings of MICCAI 1998, Lecture Notes in Computer Science*, 45:1321-8, 1999.
- [16] J. E. Downhill, M. S. Buchsbaum, J. Spiegel-Cohen T. C. Wei, E. A. Hazlett, and M. M. Haznedar. Shape and size of the corpus callosum in schizophrenia and schizotypal personality disorder. *Schizophr Res*, 42:193–208, 2000.
- [17] W. D. D'Souza, Y. Kwok, C. Deyoung, N. Zacharapoulos, M. Pepelea, P. Klahr, and C. X. Yu. Gated CT imaging using a free-breathing respiration signal from flow-volume spirometry. *Med. Phys.*, 32:3641–3649, 2005.
- [18] L. Ekberg, O. Holmberg, L. Wittgren, G. Bjelkengren, and T. Landberg. What margins should be added to the clinical target volume in radiotherapy treatment planning for lung cancer? *Radiother. Oncol.*, 48:71–77, 1998.

- [19] M. Engelsman, E. M. Damen, K. De Jaeger, K. M. van Ingen, and B. J. Mijnheer. Impact of simple tissue inhomogeneity correction algorithms on conformal radiotherapy of lung tumours. *Radiother. Oncol.*, 60:95–105, 2001.
- [20] S. C. Erridge, Y. Seppenwoolde, S. H. Muller, M. van Herk, K. De Jaeger, J. S. Belderbos, L. J. Boersma, and J. V. Lebesque. Portal imaging to assess set-up errors, tumor motion and tumor shrinkage during conformal radiotherapy of non-small cell lung cancer. *Radiother. Oncol.*, 66:75–85, 2003.
- [21] G. A. Ezzell, J. M. Galvin, D. Low, J. R. Palta, I. Rosen, M. B. Sharpe, P. Xia, Y. Xiao, L. Xing, and C. X. Yu. Guidance document on delivery, treatment planning, and clinical implementation of IMRT: Report of the IMRT subcommittee of the AAPM radiation therapy committee. *Med. Phys.*, 30:2089–2115, 2003.
- [22] M. Ferrant, A. Nabavi, B. Macq, P. M. Black, F. A. Jolesz, and R. Kikinis. Serial registration of intraoperative MR images of the brain. *Med Image Anal*, 6:337–59, 2002.
- [23] M. J. Fitzpatrick, G. Starkschall, J. A. Antolak, H. Shukla J. Fu, P. J. Keall, P. Klahr, and R. Mohan. Displacement-based binning of time-dependent computed tomography image data sets. *Med. Phys.*, 33:235–246, 2006.
- [24] E. C. Ford, G. S. Mageras, E. Yorke, and C. C. Ling. A method of measuring respiratory induced anatomic motion for radiation treatment planning. *Med. Phys.*, 30:88–97, 2003.
- [25] E. C. Ford, G. S. Mageras, E. Yorke, K. E. Rosenzweig, R. Wagman, and C. C. Ling. Evaluation of respiratory movement during gated radiotherapy using film and electronic portal imaging. *Int. J. Radiat. Oncol. Biol. Phys.*, 52:522–531, 2002.
- [26] B. A. Fraass. The development of conformal radiation therapy. Med. Phys., 22:1911–1921, 1995.
- [27] J. Gee, T. Sundaram, I. Hasegawa, H. Uematsu, and H. Hatabu. Characterization of regional pulmonary mechanics from serial magnetic resonance imaging data. *Acad Radiol*, 10:1147–52, 2003.

- [28] R. George, S. S. Vedam, T. D. Chung, V. Ramakrishnan, and P. J. Keall. The application of the sinusoidal model to lung cancer patient respiratory motion. *Med. Phys.*, 32:2850–2861, 2005.
- [29] R. George, S. S. Vedam, T. D. Chung, V. Ramakrishnan, and P. J. Keall. Synchronized moving aperture radiation therapy (SMART): Improvement of breathing pattern reproducibility using respiratory coaching. *Phys. Med. Biol.*, 51:617–636, 2006.
- [30] W. S. Gharaibeh, F. J. Rohlf, D. E. Slice, and L. E. DeLisi. A geometric morphometric assessment of change in midline brain structural shape following a first episode of schizophrenia. *Biol Psychiatry*, 48:398–405, 2000.
- [31] I. S. Grills, D. Yan, A. A. Martinez, F. A. Vicini, J. W. Wong, and L. L. Kestin. Potential for reduced toxicity and dose escalation in the treatment of inoperable non-small-cell lung cancer: A comparison of intensity modulated radiation therapy (IMRT), 3D conformal radiation, and elective nodal irradiation. *Int. J. Radiat. Oncol. Biol. Phys.*, 57:875–890, 2003.
- [32] A. Hagemann, K. Rohr, H. S. Stiehl, U. Spetzger, and J. M. Gilsbach. Biomechanical modeling of the human head for physically based, nonrigid image registration. *IEEE Trans Med Imaging*, 18:875–84, 1999.
- [33] J. Hanley, M. M. Debois, D. Mah, G. S. Mageras, A. Raben, K. Rosenzweig, B. Mychalczak, L. H. Schwartz, P. J. Gloeggler, W. Lutz, C. C. Ling, S. A. Leibel, Z. Fuks, and G. J. Kutcher. Deep inspiration breathhold technique for lung tumors: The potential value of target immobilization and reduced lung density in dose escalation. *Int. J. Radiat. Oncol. Biol. Phys.*, 45:603-611, 1999.
- [34] E. Heath, D. L. Collins, P. J. Keall, L. Dong, and J. Seuntjens. Quantification of accuracy of the ANIMAL non-linear registration algorithm for registration of 4D CT images of lung. Med. Phys. (submitted), 2007.
- [35] E. Heath and J. Seuntjens. A direct voxel tracking method for four-dimensional Monte Carlo dose calculations in deforming anatomy. *Med. Phys.*, 33:434–445, 2006.
- [36] C. L. Hector, S. Webb, and P. M. Evans. The dosimetric consequences of interfractional patient movement on conventional and intensity-modulated breast radiotherapy treatments. *Radiother. Oncol.*, 54:57–64, 2000.

- [37] M. Holden, D. L. Hill, E. R. Denton, J. M. Jarosz, T. C. Cox, T. Rohlfing, J. Goodey, and D. J. Hawkes. Voxel similarity measures for 3-D serial MR brain image registration. *IEEE Trans. Med. Imaging*, 19:94–102, 1998.
- [38] S. B. Jiang, C. Pope, K. M. Al. Jarrah, J. H. Kung, T. Bortfeld, and G. T. Y. Chen. An experimental investigation on intra-fractional organ motion effects in lung IMRT treatments. *Phys. Med. Biol.*, 48:1773–1784, 2003.
- [39] R. Kashani, K. Lam, D. Litzenberg, and J. Balter. Technical note: A deformable phantom for dynamic modeling in Radiation Therapy. Med. Phys., 34:199–201, 2007.
- [40] P. Keall. 4-dimensional computed tomography imaging and treatment planning. Semin Radiat Oncol, 14:81–90, 2004.
- [41] P. Keall and J. M. Balter. 4-dimensional computed tomography imaging and treatment planning. Semin Radiat Oncol, 14:81–90, 2004.
- [42] P. J. Keall, S. Joshi, S. S. Vedam, J. V. Siebers, V. R. Kini, and R. Mohan. Four-dimensional radiotherapy planning for DMLC-based respiratory motion tracking. *Med. Phys.*, 32:942–951, 2005.
- [43] P. J. Keall, S Joshi, S. S. Vedam, J. V. Siebers, V. R. Kini, and R. Mohan. Four-dimensional radiotherapy planning for DMLC-based respiratory motion tracking. *Med. Phys.*, 32:942–951, 2005.
- [44] P. J. Keall, V. R. Kini, S. S. Vedam, and R. Mohan. Motion adaptive x-ray therapy: a feasibility study. *Phys. Med. Biol.*, 46:1–10, 2001.
- [45] P. J. Keall, G. S. Mageras, J. M. Balter, R. S. Emery, K. M. Forster, S. B. Jiang, J. M. Kapatoes, D. A. Low, M. J. Murphy, B. R. Murray, C. R. Ramsey, M. B. Van Herk, S. S. Vedam, J. W. Wong, and E. Yorke. The management of respiratory motion in radiation oncology report of AAPM Task Group 76. Med. Phys., 33:3874-3900, 2006.
- [46] P. J. Keall, J. V. Siebers, S. Joshi, and R. Mohan. Monte Carlo as four-dimensional radiotherapy treatment-planning tool to account for respiratory motion. *Phys. Med. Biol.*, 49:3639–3648, 2004.
- [47] P. J. Keall, G. Starkschall, H. Shukla, K. M. Forster, V. Ortiz, C. W. Stevens, S. S. Vedam, R. George, T. Guerrero, and R. Mohan. Acquiring 4D thoracic

- CT scans using a multislice helical method. *Phys. Med. Biol.*, 49:2053–2067, 2004.
- [48] M. L. Kessler and M. Roberson. Image registration and data fusion for radiotherapy treatment planning. Springer-Verlag, New York, 2005.
- [49] C. H. Ketting, M. Austin-Seymour, I. Kalet, J. Unger, S. Hummel, and J. Jacky. Consistency of three-dimensional planning target volumes across physicians and institutions. *Int. J. Radiat. Oncol. Biol. Phys*, 37:445–453, 1997.
- [50] D. J. W. Kim, B. R. Murray, and R. Halperin. Held-breath self-gating technique for radiotherapy of non-small-cell lung cancer: a feasibility study. *Int. J. Radiat. Oncol. Biol. Phys*, 49:43–49, 2001.
- [51] H. D. Kubo and B. C. Hill. Respiration gated radiotherapy treatment: A technical study. *Phys. Med. Biol.*, 41:83–91, 1996.
- [52] F. J. Lagerwaard, J. R. Van Sornsen de Koste, M. R. Nijssen-Visser, R. H. Schuchhard-Schipper, S. S. Oei, A. Munne, and S. Senan. Multiple "slow" CT scans for incorporating lung tumor mobility in radiotherapy planning. Int. J. Radiat. Oncol. Biol. Phys., 51:932–937, 2001.
- [53] I. Lax. Target dose versus extratarget dose in stereotactic radiosurgery. *Acta Oncol.*, 32:453–457, 1993.
- [54] I. Lax, H. Blomgren, I. Naslund, and R. Svanstrom. Stereotactic radiotherapy of malignancies in the abdomen. Methodological aspects. Acta Oncol., 33:677– 683, 1994.
- [55] H. Lester and S. R. Arridge. A survey of hierarchical non-linear medical image registration. *Pattern Recognition*, 32:129–49, 1999.
- [56] J. G. Li and L. Xing. Inverse planning incorporating organ motion. Med. Phys., 27:1573–1578, 2000.
- [57] T. Li, E. Schreibmann, B. Thorndyke, G. Tillman, A. Boyer, A. Koong, K. Goodman, , and L. Xing. Gated CT imaging using a free-breathing respiration signal from flow-volume spirometry. *Med. Phys.*, 32:3650–3660, 2005.
- [58] D. A. Low, M. Nystrom, E. Kalinin, P. Parikh, J. F. Dempsey, J. D. Bradley, S. Mutic, S. H. Wahab, T. Islam, G. Christensen, D. G. Politte, and B. R.

- Whiting. A method for the reconstruction of four-dimensional synchronized CT scans acquired during free breathing. *Med. Phys.*, 30:1254–1263, 2003.
- [59] W. Lu, M. Chen, G. H. Olivera, K. J. Ruchala, and T. R. Mackie. Fast free-form deformable registration via calculus of variations. *Phys. Med. Biol.*, 49:3067–3087, 2004.
- [60] W Lu, P. J. Parikh, J. P. Hubenschmidt, J. D. Bradley, and D. A. Low. A comparison between amplitude sorting and phase-angle sorting using external respiratory measurement for 4D CT. *Med. Phys.*, 33:2964–2974, 2006.
- [61] F. Maes, A. Dollignon, D. Vandermeulen, G. Marchal, and P. Seutens. Multimodality image registration by maximization of mutual information. *IEEE Trans. Med. Imaging*, 16:187–98, 1997.
- [62] G. S. Mageras, A. Pevsner, E. D. Yorke, K. E. Rosenzweig, E. C. Ford, A. Hertanto, S. M. Larson, D. M. Lovelock, Y. E. Erdi, S. A. Nehmeh, J. L. Humm, and C. C. Ling. Measurement of lung tumor motion using respiration-correlated CT. Int. J. Radiat. Oncol. Biol. Phys, 60:933-941, 2004.
- [63] J. B. A. Maintz and M. A. Viergever. A survey of Medical Image Registration. *Medical Image Analysis*, 2:1–36, 1998.
- [64] S. Malone, J. M. Crook, W. S. Kendal, and J. Szanto. Respiratory induced prostate motion: Quantification and characterization. *Int. J. Radiat. Oncol. Biol. Phys.*, 48:105–109, 2002.
- [65] U. Malsch, C. Thieke, P. E. Huber, and R. Bendl. An enhanced block matching algorithm for fast elastic registration in adaptive radiotherapy. *Phys. Med. Biol.*, 51:4789–4806, 2006.
- [66] D. Mattes, D. R. Haynor, H. Vesselle, T. K. Lewellen, and W. Eubank. PET-CT image registration in the chest using free-form deformations. *IEEE Trans Med Imaging*, 22:120–8, 2003.
- [67] M. Mazonakis, J. Damilakis, H. Varveris, P. Prassopoulos, and N. Gourtsoyiannis. Image segmentation in treatment planning for prostate cancer using the region growing technique. Br J Radiol, 74:243-248, 2001.
- [68] S. D. McCarter and W. A. Beckham. Evaluation of the validity of a convolution method for incorporating tumour movement and set-up variations into the radiotherapy treatment planning system. *Phys. Med. Biol.*, 45:923–931, 2000.

- [69] S. Minohara, T. Kanai, M. Endo, K. Noda, and M. Kanazawa. Respiratory gated irradiation system for heavy-ion radiotherapy. Int. J. Radiat. Oncol. Biol. Phys., 47:1097–1103, 2000.
- [70] M. J. Murphy, J. R. Adler, M. Bodduluri, J. Dooley, K. Forster, J. Hai, Q. Le, G. Luxton, D. Martin, and J. Poen. Image-guided radiosurgery for the spine and pancreas. *Comput. Aided Surg.*, 5:278–288, 2000.
- [71] M. J. Murphy, D. Martin, R. Whyte, J. Hai, C. Ozhasoglu, and Q. T. Le. The effectiveness of breath-holding to stabilize lung and pancreas tumors during radiosurgery. *Int. J. Radiat. Oncol. Biol. Phys.*, 53:475–482, 2002.
- [72] T. Neicu, R. Berbeco, J. Wolfgang, and S. B. Jiang. Synchronized moving aperture radiation therapy (SMART): Improvement of breathing pattern reproducibility using respiratory coaching. *Phys. Med. Biol.*, 51:617–636, 2006.
- [73] T. Neicu, H. Shirato, Y. Seppenwoolde, and S. B. Jiang. Synchronized moving aperture radiation therapy (SMART): Average tumor trajectory for lung patients. *Phys. Med. Biol.*, 48:587–598, 2003.
- [74] E. Nioutsikou, J. R. N. Symonds-Tayler, J. L. Bedford, and S. Webb. Quantifying the effect of respiratory motion on lung tumour dosimetry with the aid of a breathing phantom with deforming lungs. *Phys. Med. Biol.*, 51:3359–3374, 2006.
- [75] C. Ozhasoglu and M. J. Murphy. Issues in respiratory motion compensation during external-beam radiotherapy. Int. J. Radiat. Oncol. Biol. Phys., 52:1389– 1399, 2002.
- [76] L. Papiez. The leaf sweep algorithm for an immobile and moving target as an optimal control problem in radiotherapy delivery. *Math. Comput. Model.*, 37:735–745, 2003.
- [77] L. Papiez. DMLC leaf-pair optimal control of IMRT delivery for a moving rigid target. *Med. Phys.*, 31:2742–2754, 2004.
- [78] C. A. Pelizzari, G. T. Chen, D. R. Spelbring, R. R. Weichselbaum, and C. T. Chen. Accurate three-dimensional registration of CT, PET and/or MR images of brain. J. Computer Assist. Tomogr., 13:20–26, 1989.
- [79] M. Peters. The mechanical basis of respiration. Little, Brown, and Co., Boston, 1969.

- [80] C. Plathow, C. Fink S. Ley, M. Puderbach, W. Hosch, A. Schmahl, J. Debus, and H. U. Kauczor. Analysis of intrathoracic tumor mobility during whole breathing cycle by dynamic MRI. *Int. J. Radiat. Oncol. Biol. Phys.*, 59:952–959, 2004.
- [81] J. P. W. Pluim, J. B. A. Maintz, and M. A. Viergever. Mutual-information-based registration of medical images: a survey. *IEEE Trans. Med. Imaging*, 22:986–1004, 2003.
- [82] J. A. Purdy. Advances in three-dimensional treatment planning and conformal dose delivery. Semin. Oncol., 24:655-671, 1997.
- [83] V. M. Remouchamps, N. Letts, F. A. Vicini, M. B. Sharpe, L. L. Kestin, P. Y. Chen, A. A. Martinez, and J. W. Wong. Initial clinical experience with moderate deep-inspiration breath hold using an active breathing control device in the treatment of patients with left-sided breast cancer using external beam radiation therapy. *Int. J. Radiat. Oncol. Biol. Phys.*, 56:704-715, 2003.
- [84] E. Rietzel, G. T. Chen, N. C. Choi, and C. G. Willet. Four-dimensional image-based treatment planning: Target volume segmentation and dose calculation in the presence of respiratory motion. *Int. J. Radiat. Oncol. Biol. Phys.*, 61:1535–1550, 2005.
- [85] E. Rietzel and G. T. Y. Chen. Deformable registration of 4D computed to-mography data. *Med. Phys.*, 33:4423–4430, 2006.
- [86] E Rietzel, T. Pan, and G. T. Y. Chen. Four-dimensional computed tomography: Image formation and clinical protocol. Med. Phys., 32:874–889, 2005.
- [87] A. Roche, G. Malandain, X. Pennec, and N. Ayache. The correlation ratio as a new similarity measure for multimodal image registration. *Proceedings of MICCAI 1998, Lecture Notes in Computer Science*, 1496:1115–24, 1998.
- [88] P. Rogelj and S. Kovacic. Similarity measures for non-rigid registration Proc. SPIE, 4322:569–78, 2001.
- [89] T. Rohlfing, Jr. C. R. Maurer, W. G. O'Dell, and J. Zhong. Modeling liver motion and deformation during the respiratory cycle using intensity-based nonrigid registration of gated MR images. *Med. Phys.*, 31(3):427-432, 2004.
- [90] K. Rohr. Elastic Registration of Multimodal Medical Images: A survey. Auszug aus: Kunstilche Intelligenz, 3:11–17, 2000.

- [91] C. S. Ross, D. H. Hussey, E. C. Pennington, W. Stanford, and J. F. Doornbos. Analysis of movement of intrathoracic neoplasms using ultrafast computerized tomography. *Int. J. Radiat. Oncol. Biol. Phys.*, 18:671–677, 1990.
- [92] M. Rosu, J. M. Balter, I. J. Chetty, M. L. Kessler, and D. L. McShan. How extensive of a 4D dataset is needed to estimate cumulative dose distribution plan evaluation metrics in conformal lung therapy? *Med. Phys.*, 34:233–245, 2007.
- [93] M. Rosu, I. J. Chetty, M. L. Kessler, and R. K. Ten Haken. Monte Carlo Non-Adaptive 4-D Treatment Planning in Conformal Radiation Therapy: Why, How, and What To Look For. In: Integrating New Technologies into the Clinic: Monte Carlo and Image-Guided Radiation Therapy, Medical Physics Monograph No. 32, B. H. Curran, J. E. Balter, I. J. Chetty (Eds) Proceedings of the American Association of Physicists in Medicine, Summer School, University of Windsor, Windsor, Ontario, Canada, June 18-22, 2006, Medical Physics Publishing, Madison, pp 293, Medical Physics Publishing (Madison):pp 293, June 18-22, 2006.
- [94] D. Rueckert, L. I. Sonoda, C. Hayes, D. L. Hill, M. O. Leach, and D. J. Hawkes. Nonrigid registration using free-form deformations: Application to breast MR images. *IEEE Trans Med Imag*, 18:712–721, 1999.
- [95] M. Schaefer, M. W. Munter, C. Thilmann, F. Sterzing, S. E. Combs P. Haering, and J. Debus. Influence of intra-fractional breathing movement in step-andshoot IMRT. *Phys. Med. Biol.*, 49:N175–N179, 2004.
- [96] B. Schaly, J. A. Kempe, G. S. Bauman, J. J. Battista, and J. Van Dyk. Tracking the dose distribution in radiation therapy by accounting for variable anatomy. *Phys. Med. Biol.*, 49:791–805, 2004.
- [97] A. Schweikard, G. Glosser, M. Bodduluri, M. J. Murphy, and J. R. Adler. Robotic motion compensation for respiratory movement during radiosurgery. *Comput. Aided Surg.*, 5:263–277, 2000.
- [98] Y. Seppenwoolde, H. Shirato, K. Kitamura, S. Shimizu, M. van Herk, J. V. Lebesque, and K. Miyasaka. Precise and real-time measurement of 3D tumor motion in lung due to breathing and heartbeat, measured during radiotherapy. *Int. J. Radiat. Oncol. Biol. Phys.*, 53:822–834, 2002.

- [99] S. Shimizu, H. Shirato, S. Ogura, H. Akita-Dosaka, K. Kitamura, T. Nishioka, K. Kagei, M. Nishimura, and K. Miyasaka. Detection of lung tumor movement in real-time tumor-tracking radiotherapy. *Int. J. Radiat. Oncol. Biol. Phys.*, 51:304–310, 2001.
- [100] H. Shirato, S. Shimizu, T. Kunieda, K. Kitamura, M. van Herk, K. Kagei, T. Nishioka, S. Hashimoto, K. Fujitaa, H. Aoyama, K. Tsuchiya, K. Kudo, and K. Miyasaka. Physical aspects of a real-time tumor-tracking system for gated radiotherapy. *Radiother. Oncol.*, 48:1187–1195, 2000.
- [101] K. E. Sixel, M. Ruschin, R. Tirona, and P. C. Cheung. Digital fluoroscopy to quantify lung tumor motion: potential for patient-specific planning target volumes. *Int. J. Radiat. Oncol. Biol. Phys.*, 57:717–723, 2003.
- [102] C. W. Stevens, R. F. Munden, K. M. Forster, J. F. Kelly, Z. Liao, G. Starkschall, S. Tucker, and R. Komaki. Respiratory-driven lung tumor motion is independent of tumor size, tumor location, and pulmonary function. *Int. J. Radiat. Oncol. Biol. Phys.*, 51:62–68, 2001.
- [103] C. Studholme, D. L. G. Hill, and D.J. Hawkes. An overlap invariant entropy measure of 3D medical image alignment. *Pattern Recognition*, 32:71–86, 1999.
- [104] Y. Suh, B. Yi, S. Ahn, J. Kim, S. Lee, S. Shin, S. Shin, and E. Choi. Aperture maneuver with compelled breath (AMC) for moving tumors: A feasibility study with a moving phantom. *Med. Phys.*, 31:760–766, 2004.
- [105] H. D. Suit. Potential for improving survival rate for the cancer patient by increasing the efficacy of the treatment of the primary tumor. Cancer, 50:1227– 1234, 1982.
- [106] R. W. Underberg, F. J. Lagerwaard, B. J. Slotman, J. P. Cuijpers, and S. Senan. Use of maximum intensity projections (MIP) for target volume generation in 4DCT scans for lung cancer. *Int. J. Radiat. Oncol. Biol. Phys.*, 63:253–260, 2005.
- [107] P. A. Van den Elsen, E. J. D. Pol, and M. A. Viergever. Medical image matching a review with classification. *IEEE Eng. Med. Biol*, 12:26–39, 1993.
- [108] M. van Herk and H. M. Kooy. Automatic three-dimensional correlation of CT-CT, CTMRI, and CT-SPECT using chamfer matching. Med. Phys., 21:1163–1178, 1994.

- [109] J. R. van Sornsen de Koste, F. J. Lagerwaard, R. H. Schuchhard-Schipper, M. R. Nijssen-Visser, P. W. Voet, S. S. Oei, and S. Senan. Dosimetric consequences of tumor mobility in radiotherapy of stage I non-small cell lung cancer - an analysis of data generated using "slow" CT scans. Radiother. Oncol., 61:93-99, 2001.
- [110] S. S. Vedam, P. J. Keall, V. R. Kini, H. Mostafavi, H. P. Shukla, and R. Mohan. Acquiring a four-dimensional computed tomography dataset using an external respiratory signal. *Phys. Med. Biol.*, 48:45–62, 2003.
- [111] S. S. Vedam, V. R. Kini, P. J. Keall, V. Ramakrishnan, H. Mostafavi, and R. Mohan. Quantifying the predictability of diaphragm motion during respiration with a noninvasive external marker. *Med. Phys.*, 30:505–513, 2003.
- [112] H. Wang, L. Dong, J. O'Daniel, R. Mohan, A. S. Garden, K. K. Ang, D. A. Kuban, M. Bonnen, J. Y. Chang, and R. Cheung. Validation of an accelerated 'demons' algorithm for deformable image registration in radiation therapy. *Phys. Med. Biol.*, 50:2887–2905, 2005.
- [113] S. Webb. The effect on IMRT conformality of elastic tissue movement and a practical suggestion for movement compensation via the modified dynamic multileaf collimator (dMLC) technique. *Phys. Med. Biol.*, 50:1163–1190, 2005.
- [114] S. Webb. Limitations of a simple technique for movement compensation via movement-modified fluence profiles. *Phys. Med. Biol.*, 50:N155–N161, 2005.
- [115] J. W. Wong, M. B. Sharpe, D. A. Jaffray, V. R. Kini, J. M. Robertson, J. S. Stromberg, and A. A. Martinez. The use of active breathing control (ABC) to reduce margin for breathing motion. *Int. J. Radiat. Oncol. Biol. Phys.*, 44:911–919, 1999.
- [116] R. P. Woods, S. T. Grafton, C. J. Holmes, S. R. Cherry, and J. C. Mazziotta. Automated image registration: I. General methods and intrasubject, intramodality validation. J. Comput. Assist. Tomogr., 22:139–52, 1998.
- [117] R. P. Woods, S. T. Grafton, C. J. Holmes, S. R. Cherry, and J. C. Mazziotta. Automated image registration: II. General methods and intrasubject, intramodality validation. *J. Comput. Assist. Tomogr.*, 22:139–52, 1998.
- [118] E. D. Yorke, Z. Fuks, L. Norton, W. Whitmore, and C. C. Ling. Modelling the development of metastases from primary and locally recurrent tumors:

- comparison with a clinical data base of prostate cancer. $Cancer\ Res.,\ 53:2987-2993,\ 1993.$
- [119] M. J. Zelefsky, Z. Fuks, and S. A. Leibel. Intensity-modulated radiation therapy for prostate cancer. *Semin. Radiat. Oncol.*, 12:229–237, 2002.

Index

Alleviating breathing motion effects			7
Breath hold techniques - Active breathing control (ABC)			7
Breath hold techniques - Voluntary			7
Incorporation techniques - Four-dimensional radiotherapy (4D RT)			8
Incorporation techniques - Inhalation and exhalation breath hold CT	sca	ans	8
Incorporation techniques - Slow CT			8
Respiratory gating			7
Shallow breathing - Abdominal pressure			7
Shallow breathing - Voluntary			7
Deformable lung phantom at MGH			62
3D motion and motion reproducibility		69,	70
Assessment of image registration accuracy		76,	84
CT data acquisition			65
Deformable image registration			73
Simulation of lung tissue		63,	67
Dynamic phantoms		9,	54
Deformable lung phantoms		58,	61
Deformable phantoms		9,	55
Rigid lung phantoms			60
Rigid phantoms	54,	55,	58
Effects of the respiratory motion			3
On delivery			5, 6
Blurring effect			5
Interface effect			6
Interplay effect			6
Shift of the dose distribution			5
On imaging	4,	18,	20
On planning			4

Four-dimensional radiotherapy procedure (4D RT)				12
Four-dimensional computed tomography (4D CT)				12
Amplitude based reconstruction method			17,	18
Ciné acquisition method				13
Helical acquisition method				15
Phase (time) based reconstruction method			16	-18
Four-dimensional treatment delivery (4D TD)				23
Four-dimensional treatment planning (4D TP)				19
Adaptive delivery				22
Non-adaptive delivery				20
Image registration techniques				25
ANIMAL algorithm			37,	71
Blurred image intensity				38
Image gradient magnitude				38
Linear registration		39,	42,	46
Non-linear registration		42,	44,	46
Classification				26
Affine		28,	33,	39
Atlas				28
Intersubject				28
Intrasubject				28
Monomodal			27,	29
Multimodal			27,	29
Non-rigid (deformable)	8,	28,	30,	34
Rigid		28,	33,	39
Optimization methods				35
ANIMAL				46
Similarity measures				31
Correlation coefficient		344,	45,	74
Correlation ratio			31,	33
Mutual information			31,	33
Sum of squared differences				31
Transformation models				33
Elastic model			34,	37
Finite element model (FE)				35
Spline based				34
Viscous model				35

Validation		36,	75
Comparison with a known deformation field		37,	75
Consistency test		37,	75
Distance-to agreement (DTA) of identical landmarks		36,	75
Distance-to agreement of 3D surfaces	37,	75,	78
Image similarity metrics based		37,	75
Visual inspection		36,	75
Modern approaches to radiation therapy			1
Image-guided radiotherapy (IGRT)			3
Intensity-modulated radiation therapy (IMRT)			2
Three-dimensional conformal radiotherapy (3D CRT)			1

List of Abbreviations

3D CRT: Three-dimensional conformal radiation therapy

3D CT: Three-dimensional computed tomography

4D CT: Four-dimensional computed tomography

4D RT: Four-dimensional radiotherapy

4D TD: Four-dimensional treatment delivery

4D TP: Four-dimensional treatment planning

ABC: Active breathing control

ANIMAL: Automated nonlinear matching and anatomical labeling

AP: Anterior-posterior

CC: Correlation coefficient

COM: Center of mass

CT: Computed tomography

CTV: Clinical target volume

DIR: Deformable image registration

DTA: Distance-to-agreement

EE: Early Exhale

EI: Early Inhale

FE: Finite element

fMRI: Functional magnetic resonance imaging

FWHM: Full-width-half-max

GTV: Gross tumor volume

ICRU: International Commission on Radiation Units and Measurements

IMRT: Intensity-modulated radiation therapy

kV CT: Kilovoltage CT

LE: Late Exhale

LI: Late Inhale

LM: Landmark

ME: Mid Exhale

MI: Mid Inhale

MI: Mutual information

MLC: Multileaf collimator

MRI: Magnetic resonance imaging

MV CT: Megavoltage CT

NMI: Normalized mutual information

OR: Organ at risk

PD: Planning dataset

PE: Peak Exhale

PET: Positron emission tomography

PI: Peak Inhale

PTV: Planning target volume

RL: Right-left

RPM: Varian's real-time position management respiratory gating system

SD: Standard deviation

SI: Superior-inferior

SPECT: Single photon emission computed tomography

SSD: Sum of squared differences

TCP: Tumor control probability

TPE: Thermoplastic elastomer

US: Ultrasound